machines

Article

Study on Aerodynamic Drag Reduction by Plasma Jets for 600 km/h Vacuum Tube Train Sets

Ang Li [1], Hongjiang Cui [1], Ying Guan [1,*], Jichen Deng [2], Ying Zhang [2] and Wu Deng [3,4]

1 School of Locomotive and Rolling Stock Engineering, Dalian Jiaotong University, Dalian 116028, China; liang121417@foxmail.com (A.L.); chj@djtu.edu.cn (H.C.)
2 New Product Development Department, CRRC DALIAN Co., Ltd., Dalian 116021, China; dengjichen.dl@crrcgc.cc (J.D.)
3 School of Electronic Information and Automation, Civil Aviation University of China, Tianjin 300300, China; wdeng@cauc.edu.cn
4 Traction Power State Key Laboratory, Southwest Jiaotong University, Chengdu 610031, China
* Correspondence: guanying2017@djtu.edu.cn

Abstract: In order to break through the speed bottleneck, researchers envision using tubes to cover high-speed maglev trains and extract some of the air inside the tubes, creating a low-density environment on the ground, greatly reducing the aerodynamic drag of the trains, and in a relatively economical and feasible way, making high subsonic (600 km/h and above) and even supersonic ground transportation possible. The faster the running speed of high-speed trains, the greater the impact of aerodynamic drag on their energy consumption. Studying the aerodynamic characteristics of trains with a speed of 600 km/h can help optimize the aerodynamic shape of the train, reduce aerodynamic drag, and reduce energy consumption. This has positive implications for improving train energy efficiency, reducing energy consumption, and environmental impact. This paper adopts the numerical simulation method to study the drag reduction effect of the plasma arrangement and different excitation speeds on the train set in four positions when the incoming wind speed is 600 km/h, to analyze the mechanism of drag reduction, and then to analyze the combination of working conditions in order to investigate the drag reduction effect of plasma on the vacuum tube train set with an ambient pressure of 10,000 Pa. The findings demonstrate that the plasma induces the directional flow of the gas close to the wall to move the flow separation point backward and delay the separation of the flow, thereby reducing the front and rear differential pressure drag of the train set and lowering the aerodynamic drag coefficient of the entire train. The plasma arrangement is located at the rear of the flow separation point and in close proximity to the flow separation point. The pneumatic drag reduction effect peaks when the excitation speed reaches 0.2 times the train speed and the pneumatic drag reduction ratio is around 0.88%; the pneumatic drag reduction ratio of the rear car peaks when the excitation speed reaches 0.25 times the train speed and the pneumatic drag reduction ratio is 1.62%. The SDBD (Surface Dielectric Barrier Discharge) device is installed at the flow separation point around the nose tip of the rear car.

Keywords: train aerodynamics; vacuum tube; plasma; active flow control; railway technology

Citation: Li, A.; Cui, H.; Guan, Y.; Deng, J.; Zhang, Y.; Deng, W. Study on Aerodynamic Drag Reduction by Plasma Jets for 600 km/h Vacuum Tube Train Sets. *Machines* **2023**, *11*, 1078. https://doi.org/10.3390/machines11121078

Received: 4 October 2023
Revised: 27 November 2023
Accepted: 4 December 2023
Published: 8 December 2023

1. Introduction

The traditional approaches to enhancing the aerodynamic performance of trains, such as optimizing the shape of the head and rear cars [1–7], designing train bogies, pantographs, and windshield structures rationally, and other local structural optimization [8–15], have tended to be perfect and mature, subject to limitations imposed by the need to continuously improve the manufacturing process and design requirements, and gradually reveal their limitations. Scientists started devoting their time to investigating new kinds of drag reduction techniques as a result [16–22].

Vacuum tube transport combines vacuum tube technology with high-speed train technology to create a new type of surface rail transport. The vacuum tube allows the train to operate in low-density, low-pressure conditions and without external environmental disturbances, theoretically minimizing the train's operating drag [23].

Due to the viscosity and speed of air, when high-speed trains operate in the thin air tube, air will generate friction with the tube wall and train surface, and a high-pressure area and low-pressure area will be generated at the front and rear of the train, respectively. The difference in pressure generated at the front and rear of the train will hinder the high-speed operation of the train [24].

The purpose of reducing drag on vacuum tube high-speed trains is to effectively reduce energy loss, improve energy efficiency and speed during high-speed operation. In a vacuum tube, by reducing collisions between gas molecules and trains, the aerodynamic drag of the train can be reduced, allowing the train to travel farther or at a faster speed under a given energy. This drag reduction technology is very important in high-speed transportation, as it can improve transportation efficiency and reduce energy consumption. In order to further reduce aerodynamic drag and reduce operational energy consumption, domestic and foreign scholars have conducted research on train shape optimization [25,26] and tube structure design [27,28].

Surface dielectric barrier discharge (SDBD) is one of the active drag reduction techniques for turbulent flow fields that improves aerodynamic performance without altering the shape of the object by applying the proper energy excitation [29]. It is currently most frequently used in the field of aircraft flow control.

Zhang et al. investigated the flow separation control effect of SDBD on devices with different angles of attack, and showed that SDBD can effectively inhibit the width of the airflow separation zone when the angle of attack is less than 20° [30], and Yang Bo et al. carried out experimental research on the inhibition of airfoil flow separation by SDBD devices under different incoming wind speeds and angles of attack, and the results showed that SDBD can effectively inhibit the airfoil flow separation under low flow speed and large angle of attack [31]; the results also showed that SDBD can effectively inhibit the airfoil flow separation under low flow speed and large angle of attack [32]. In a separation study [31], Che et al. simulated the effect of high-altitude SDBD on wing lift coefficient, and the results showed that the wing lift coefficient can be effectively improved after the excitation of SDBD [32]. Orlov et al. simulated the phenomenon of SDBD inhibition of airflow separation under different angles of attack using simulation. The simulation results show that SDBD can effectively control flow separation [33].

There have also been some studies on cars and moving trains. Zhou et al. applied the SDBD device to a car body and analyzed the flow separation and drag reduction effect by performing flow field simulation calculations on the GTS (Ground Transportation System) model [34,35]. However, research on the SDBD device applied to the airflow control of trains is still in its infancy. Based on tests, Gao [36] examined the flow control effects of variously shaped electrodes on train models.

The shortcomings of current research lie in the lack of relevant research on plasma surface dielectric barrier discharge in train drag reduction, as well as active control jet drag reduction research on low vacuum tube high-speed trains. The Shyy model is used to simulate the plasma in this study, which uses along-surface dielectric blocking discharge technology, to examine the flow control effects of various electrode placements and excitation speeds on a model of a high-speed moving train with vacuum tubes. Simultaneously, the N-S equation is used to determine the flow field surrounding the moving train model, and the effects of excitation voltage and incident velocity on the SDBD device's ability to reduce drag are examined and contrasted. In this study, numerical computation techniques are used to analyze the structure of the flow field surrounding the fast-moving train and the features of aerodynamic drag.

2. Numerical Calculation Model

2.1. Geometric Model and Simulation Conditions

In this paper, CRH380CL, manufactured by CRRC Changchun Railway Vehicles Co., Ltd. in Changchun, China, is selected as the simulation model, the computational domain is selected, and the corresponding mesh is divided in the 2022 R1 version of ICEM CFD software provided by ANSYS, Inc. (Canonsburg, PA, USA). As shown in Figure 1a,b, the characteristic height of the train model is H = 3.8 m. The distance between the train head and the tube inlet is 9 H, the distance between the train tail and the tube outlet is 21 H, and the distance between the train bottom and the tube bottom is 0.074 H. The cross-sectional size of the tube is 1.58 H × 1.58 H. In this article, the blocking ratio of the vacuum tube is 0.356. At this point, using a low vacuum tube with a rectangular cross-section for simulation has no significant impact on the simulation results, and the influence of the tube cross-section shape on aerodynamic drag can be ignored [37].

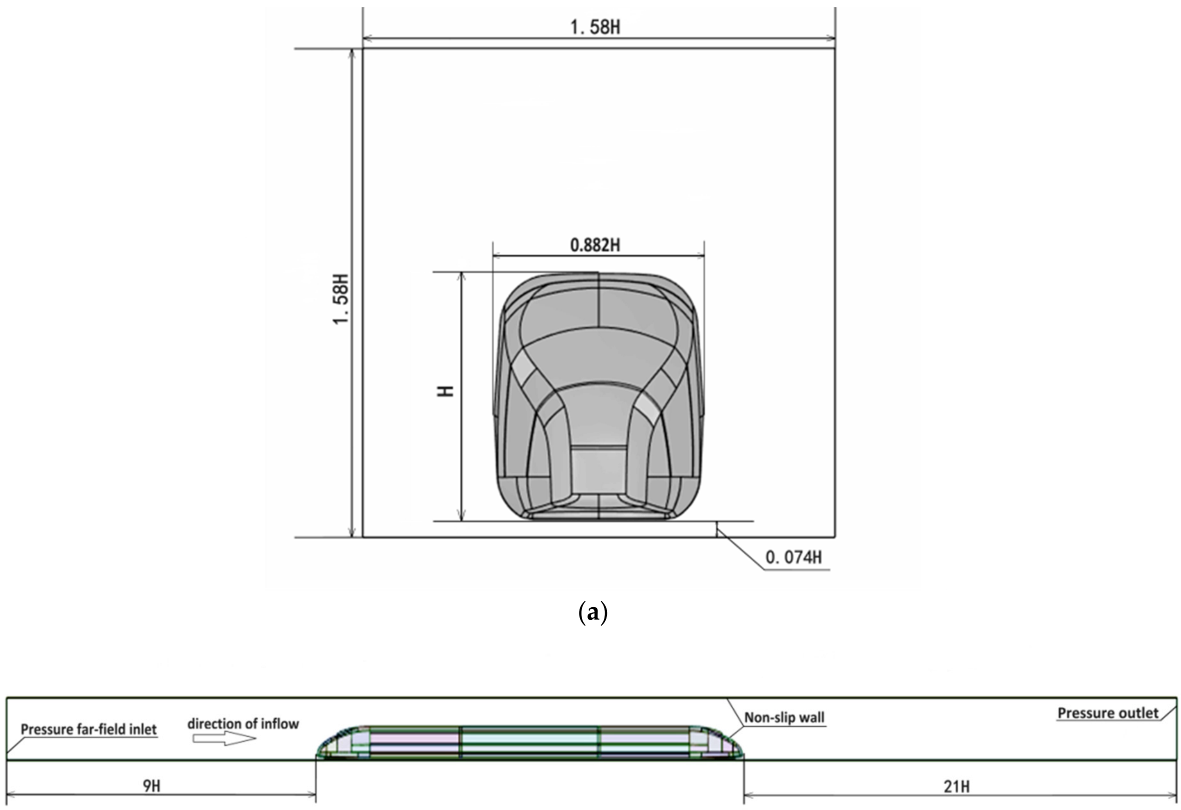

Figure 1. Simulated train model: (**a**) front view; (**b**) side view and boundary conditions.

The boundary conditions at the inlet and outlet of the tube are shown in Figure 1b. In the simulation of the vacuum tube transportation system in this article, it is assumed that the high-speed train unit is stationary. On this basis, a double precision calculation method is used to iteratively calculate in Fluent R13 software. The simulation boundary conditions are shown in Table 1.

Table 1. Simulation boundary conditions.

Computational Domain	Boundary Condition	Calculation Settings
Tube inlet	Pressure far field	0.489 Ma
Tube outlet	Pressure outlet	0
Train body	Wall	No-slip
Tube	Wall	167 m/s

The tube environment simulated in this paper is the operating environment of a moving train under a certain degree of vacuum, which is an environment with compressible air and a strong degree of turbulence, so the COUPLE algorithm coupled with pressure and velocity is selected, and the second-order windward format is chosen for each control equation to ensure the convergence of the results [38–40].

2.2. Validation of Numerical Plasma Simulation

For the dielectric blocking discharge plasma model, a simplified model of the equation of the plasma effect on the flow field proposed by Shyy et al. [41] is used, and the flow control effect of the plasma under the test condition is written as the following equation, taking into account the plasma excitation voltage, frequency, and pole-plate geometry:

$$F_x = \theta\alpha\rho_c e_c E_x \Delta t\delta \tag{1}$$

$$F_y = \theta\alpha\rho_c e_c E_y \Delta t\delta \tag{2}$$

$$E = U/d \tag{3}$$

In the above equations, θ is the alternating current frequency, taken as 7.5 kHz; α is the effective coefficient of elastic collision, taken as 1; ρ_c is the charge number density; U is the excitation voltage; e_c is the charge constant, that is, the electronic charge, taken as 1.6×10^{-19} C; Δt is the unit cycle of the effective breakdown of air time, that is, discharge time, taken as 67; E is the strength of the electric field; δ is the Dirac delta function, which is used to calculate the electric field's range. When the electric field strength is greater than the threshold value of the degree of air breakdown, the Clarke function, which is used to calculate the range of the electric field, is taken as 1, and in the opposite case, it is taken as 0.

Equations (1)–(3) are added to the N-S equation in the form of a volumetric force as a source term, which is programmed to be written as a user-defined function (UDF) and loaded into the Fluent software to achieve the purpose of simulating the plasma's impact on the flow field.

A three-dimensional rectangular cavity model is selected for the validation of plasma numerical simulation, with the ground as the plasma layout location. The longitudinal mid-section of the geometric model is shown in Figure 2.

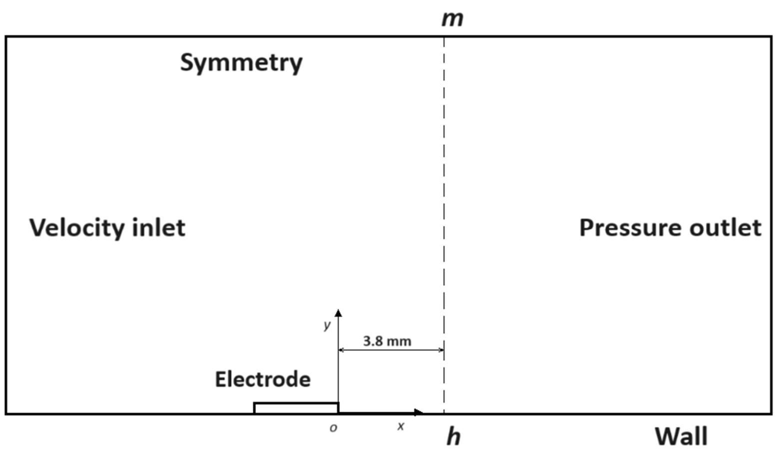

Figure 2. Longitudinal mid-section of geometric model.

Because of the generation of plasma and the movement of the core area under the action of electromagnetic fields, the size of which is 3 mm × 1.5 mm, it is necessary to encrypt the grid at the place where the plasma is generated. In this paper, the minimum size at this place is taken as 0.1 mm, so that there is a large enough grid in this area to show a trend of plasma-induced wind speed attenuation as it moves away from the electrode plate. The simulation boundary conditions are shown in Table 2.

Table 2. Boundary conditions for plasma numerical simulation.

Computational Domain	Boundary Condition	Calculation Settings
Inlet	Velocity inlet	2–10 m/s
Outlet	Pressure outlet	0
Side surface	Wall	symmetry
Bottom surface	Wall	Fixed wall

Due to the fact that the core region of the plasma is mostly located inside the boundary layer, in order to accurately describe the control effect of the plasma on the near wall flow, the turbulence model is selected as the SST (Shear Stress Transfer) k-ω model. The simulated velocity contour and vector of the longitudinal mid-section at a wind speed of 2 m/s are shown in Figure 3.

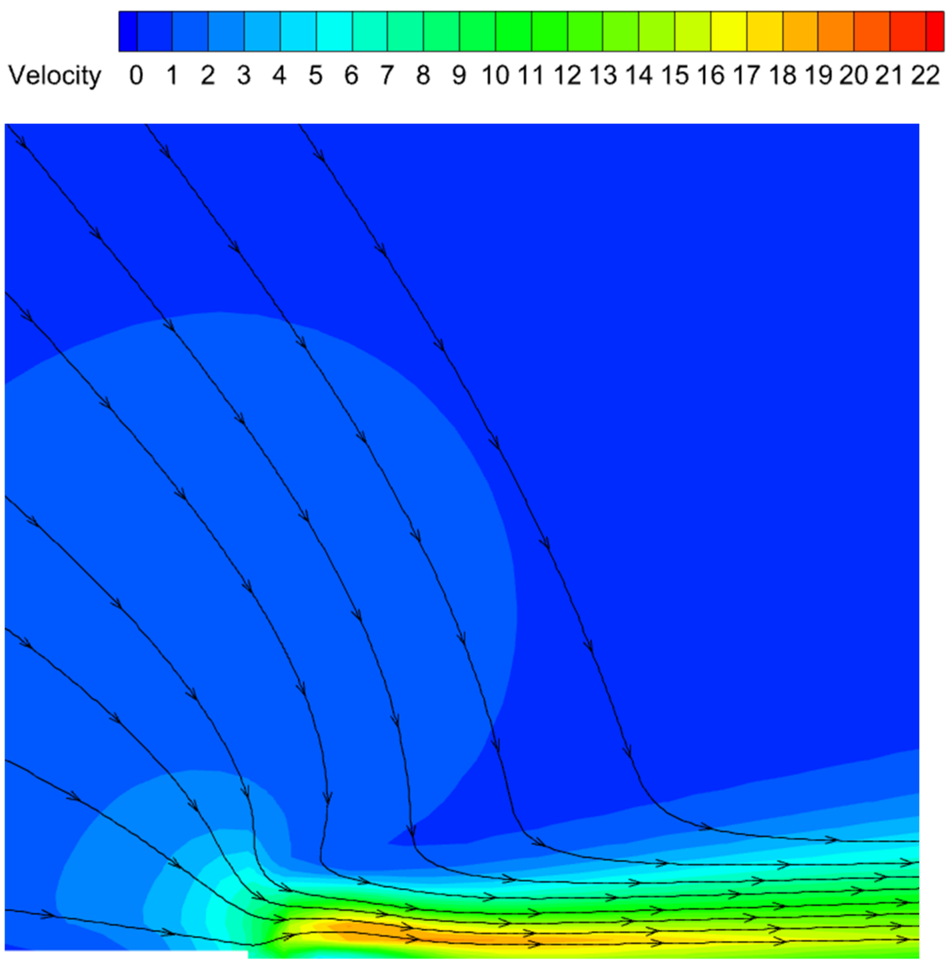

Figure 3. Longitudinal mid-section simulation with velocity contour and streamline.

From Figure 3, it can be seen that the effect of arranging the plasma is to induce a horizontal rightward airflow with a certain velocity near the wall, and the induced velocity is the highest at the plasma arrangement position; as the flow develops backwards, the velocity value gradually decreases.

To verify the accuracy of the simulation results, a line perpendicular to the longitudinal centerline of the ground is drawn 3.8 mm to the right of the plasma layout position, as shown in Figure 2 with a dashed line *mh*. Monitor the velocity distribution along the y-axis on this dashed line *mh* under various incoming wind speeds, and the obtained results are compared with the results in reference [41]. The obtained results are shown in Figure 4. In Figure 4, u represents the velocity value on the dashed line *mh*, and V_∞ is the free flow velocity from the velocity inlet.

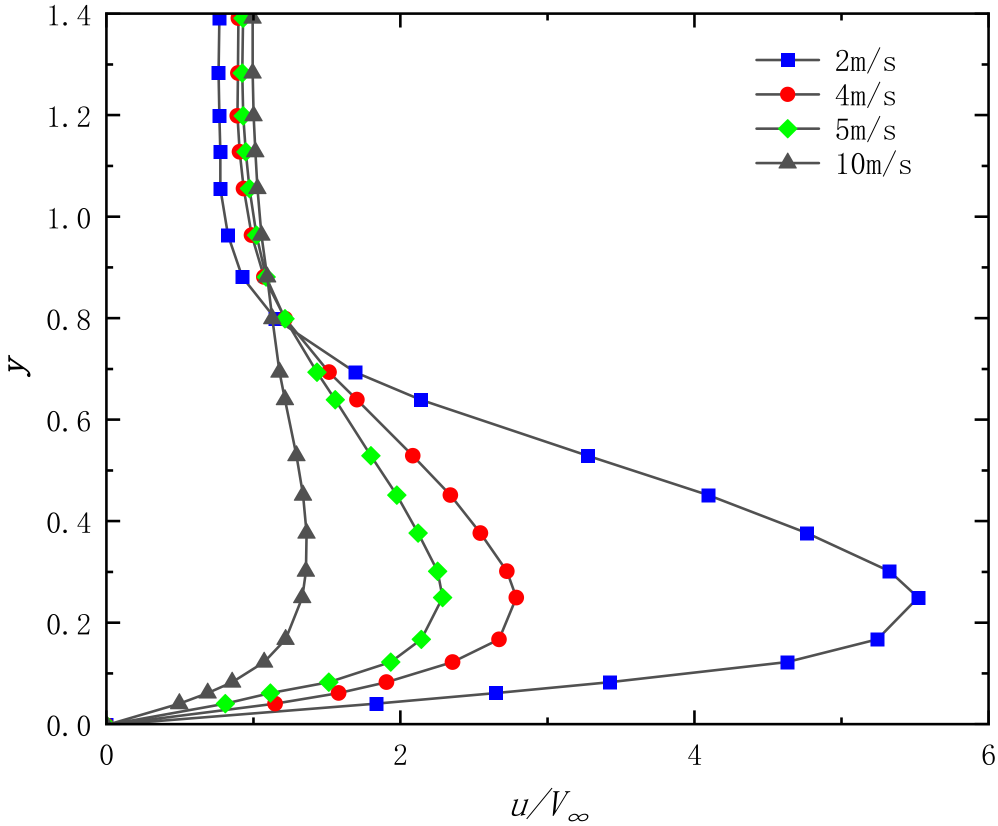

Figure 4. Comparison of simulation results.

From Figure 4, it can be seen that the simulation results in this article are basically consistent with the results in reference [41], and the error of the induced maximum wind speed at each incoming wind speed is within 3%, thus verifying the accuracy of plasma simulation in this article.

2.3. Knudsen Number

When $Re > 4000$, the flow field within the vacuum tube transport system is considered to be turbulent. The Reynolds number can be expressed as follows [42]:

$$t\,Re = \frac{\rho v D}{\mu} \tag{4}$$

where ρ is the air density in the tube; ν is the operating speed of the train set; D is the characteristic length of the tube; μ is the aerodynamic viscosity.

The simulation uses a running speed of 600 km/h for the train set and a minimum characteristic length of 6.004 m for the tube. Substituting the relevant data into Equation (4) to obtain the minimum Reynolds number results in the following:

$$Re = 6.31 \times 10^6 > 4000 \tag{5}$$

It can be concluded that the air flow within the vacuum tube transport system belongs to turbulent flow; this paper chooses the *Realizable* $k-\varepsilon$ model in the Fluent simulation. For a low vacuum and high flow rate in the vacuum tube transport system, the *Realizable* $k-\varepsilon$ model results are more in line with the real situation [37]. In order to determine whether the gas inside the tube is appropriate for the continuum medium model, which is often assessed using the Knudsen number K_{n}, it is important to check the air pressure inside the vacuum tube transportation system, which is rather low and can be expressed as [43]

$$K_n = \lambda / L \tag{6}$$

In the equation, λ is the molecular mean free range; L is the length of the characteristic length taken to simulate the length of the rolling stock [44].

The vacuum tube air in the case of 10,000 Pa and 300 K has a molecular mean free range $\lambda = 6.21 \times 10^{-7}$, the characteristic length to take the height of the rolling stock, and characteristic length dimensions of $L = 3.8$ m. Substituting Equation (6) to obtain the Knudsen number results in the following:

$$K_n = 1.63 \times 10^{-7} < 0.01 \tag{7}$$

Therefore, the air inside the vacuum tube is still a continuous medium. In this paper, the moving train travels at a speed of 600 km/h $\approx$ 0.489 *Ma*, and the air flow inside the tube is treated as compressible [45,46].

2.4. Dimensionless Coefficients

For comparison purposes, the analysis was carried out using dimensionless coefficients specifically defined in Equations (8) to (10):

$$C_{\mathrm{d}} = \frac{F_{\mathrm{d}}}{0.5\rho U^2 S} \tag{8}$$

$$C_{\mathrm{p}} = \frac{p}{0.5\rho U^2} \tag{9}$$

$$\eta = \frac{C_{\mathrm{d\,original}} - C_{\mathrm{d\,plasma}}}{C_{\mathrm{d\,original}}} \times 100\% \tag{10}$$

where η represents the rate of drag reduction ratio; C_{d} represents the aerodynamic drag coefficient; C_{P} represents the pressure coefficient; F_{d} represents the aerodynamic drag of the moving train; ρ represents the fluid density, ρ = 0.1161 kg/m^3; U represents the velocity of the distant incoming flow; S is the area of the windward surface; p is the pressure at a point in the flow field.

2.5. Reliability Analysis and Mesh Partitioning Strategy

Because the degree of grid sparsity has a greater impact on the results of numerical calculations, in order to ensure the accuracy of the calculation requirements, while taking into account the economic rationality of computational resources and improving the efficiency of the calculation and cost savings, this paper uses the rough mesh, medium mesh, and fine mesh of the three different mesh densities to demonstrate the irrelevance of the validation of the three densities of the mesh parameters, as shown in Table 3.

Table 3. Grid-independent validation.

Mesh Density	Coarse	Medium	Fine
Mesh density (10^6)	14	25	45
Aerodynamic drag coefficient C_d	0.5250	0.5130	0.5129

The numerical simulation of the subsequent high-speed trains will be conducted on the basis of a medium-density grid. In addition, in order to make the grid more body-fitting, triangular unstructured grids are used on the train surface, tetrahedral unstructured grids are used on the fluid domain, and encryption is performed on the surrounding fluid domain of the rear car, as shown in Figure 5a–c. After verifying the independence of the grid, it was found that the minimum grid size of the outer surface grid of the train was 10 mm, which could meet the simulation accuracy requirements. We set the boundary layer to 12 layers with a growth rate of 1.2 to capture the shear layer and separated the flow near the surface of the high-speed train unit. As shown in Figure 5d, a boundary layer grid (prism layer) is set near the body wall, and the height of the grid in the first layer of the body wall is set to 1.4818 mm to ensure y + ≥30, which is within the appropriate range of the corresponding turbulence model.

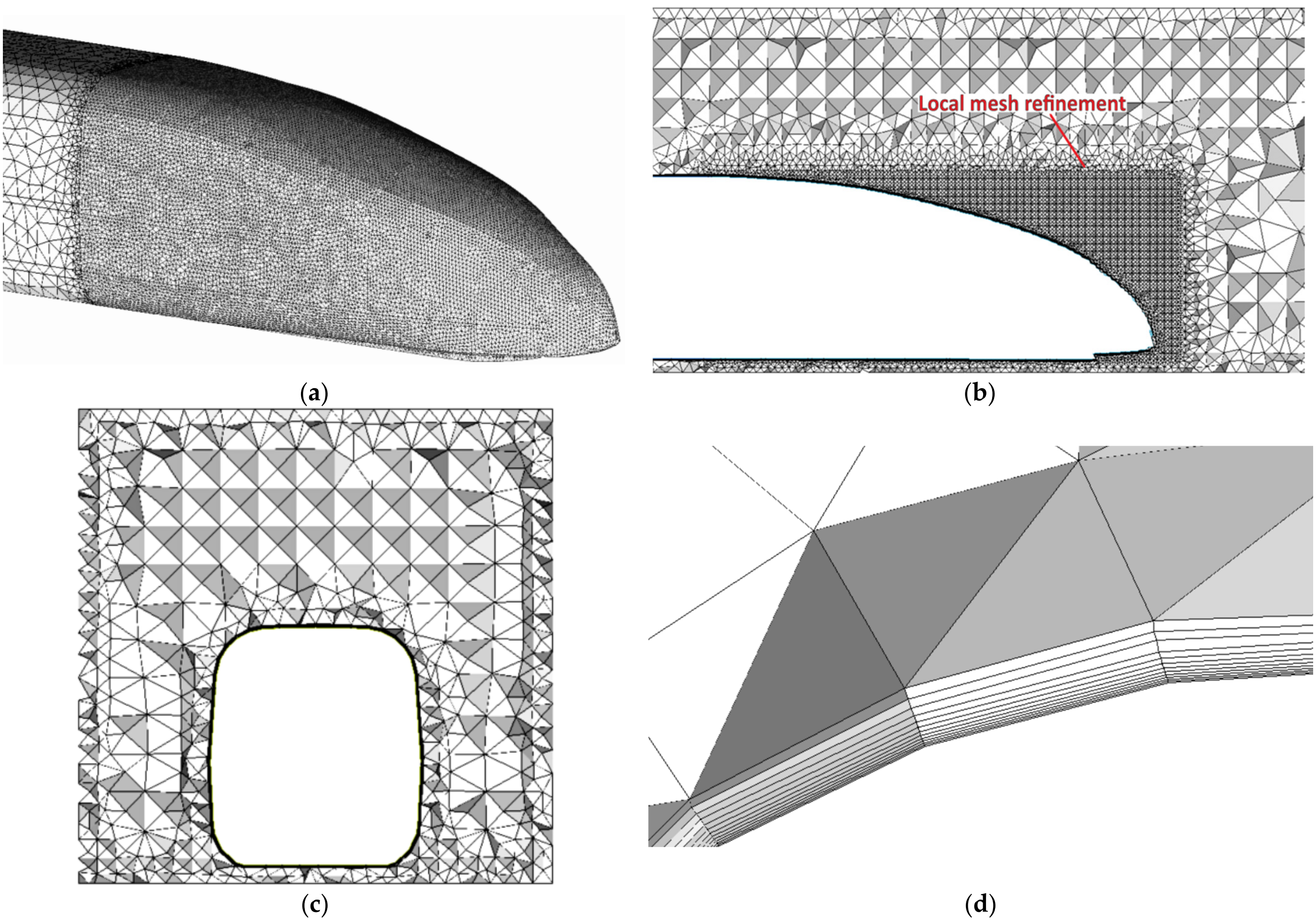

Figure 5. Model grid scheme: (**a**) surface grid division of high-speed train unit; (**b**) grid division of the watershed near the rear car; (**c**) internal grid division of vacuum tube; (**d**) boundary layer grid.

2.6. Validation of Mathematical Techniques

The accuracy of the numerical calculation method in this paper is verified by using the results of wind tunnel tests in reference [47], and a numerical calculation model for the CRH3 high-speed multiple unit is established. The wind tunnel test adopts a 1:8 three-car high-speed train model, as shown in Figure 6a. Among them, the boundary conditions and fluid domain mesh division for wind tunnel experimental simulation calculation are shown in Figure 6a,b, and the wind speed in the simulation calculation is consistent with the 250 km/h operating condition in the wind tunnel tests. To ensure that the grid density does not affect the accuracy of the numerical calculation method used in the validation, three different specifications of grids were used in the validation.

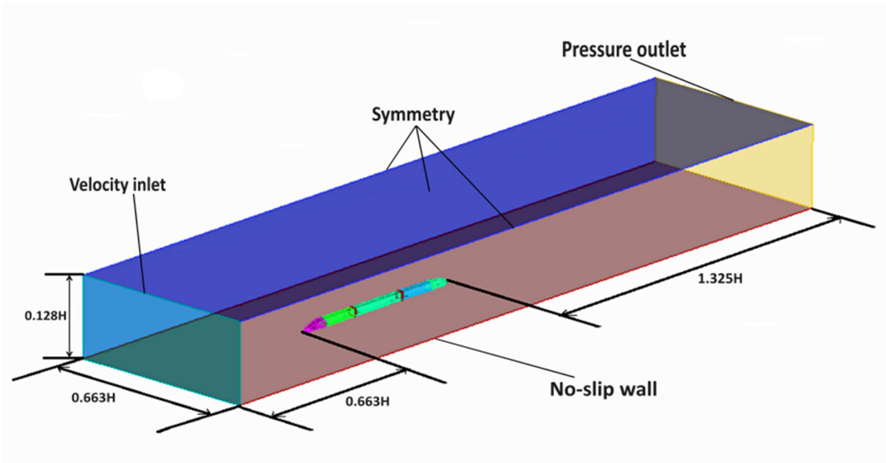

(**a**)

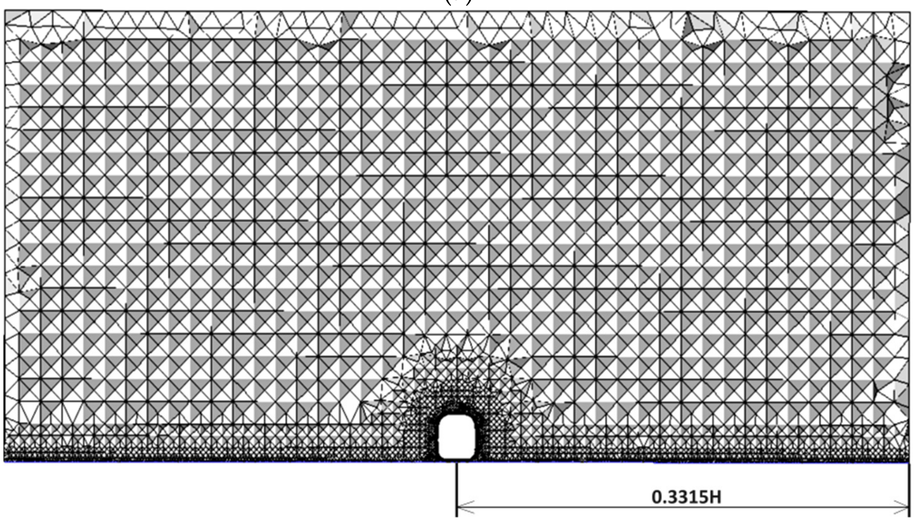

(**b**)

Figure 6. Numerical model for wind tunnel test: (**a**) numerical model and boundary conditions for wind tunnel test; (**b**) fluid domain of wind tunnel simulation.

The aerodynamic drag coefficients for the entire train in the wind tunnel test and in the numerical simulation are shown in Table 4, along with the numerical calculation's inaccuracies in comparison to the wind tunnel test. Table 4 compares samples with various grid densities as well as the outcomes of wind tunnel tests. Since the table shows that the deviation of the drag coefficients calculated by mesh simulation under various densities from the experimental results is less than or equal to 10%, the numerical simulation method used in this paper, which uses the meshes chosen, can be taken as credible.

Table 4. Validation of numerical methods.

Grid Density (Million)	9	16	28	33	Experimental
Pneumatic drag coefficient C_d	0.321	0.3	0.318	0.343	0.335
inaccuracies	4%	10%	5%	−2%	-

3. Discussion

Determination of SDBD Position at the Rear of the High-Speed Train

Analysis of the vacuum tube transport system's pressure field reveals that as rolling stock moves through the tube, a complex turbulent flow field is created. The pressure contour of the surface of the rolling stock in the vacuum tube transportation system is illustrated in Figure 7. The pressure on the surface of the body of the rolling stock is not the same and it varies substantially in different portions of the rolling stock.

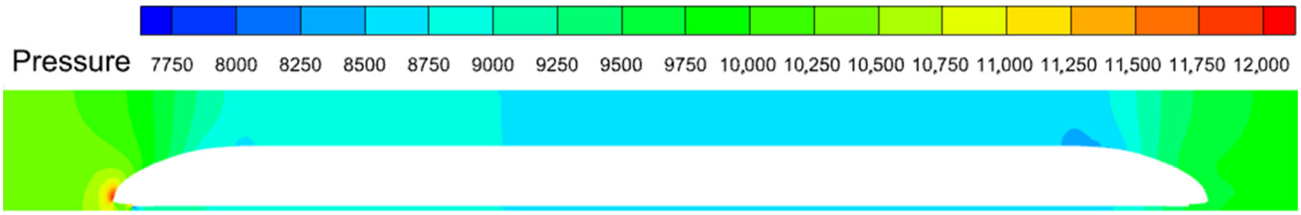

Figure 7. Pressure contour for longitudinal mid-section of the original entire train.

When Figure 7 is analyzed, it is clear that the rolling stock operating in a tube will create a complex turbulent flow field and that the surrounding air flow state is quite complicated. The pressure on the surface of the rolling stock's body varies greatly depending on where it is located; during vacuum tube driving, the closed tube's function causes the surrounding air flow velocity to accelerate, which causes the front of the train to constantly push the air in front of it, compressing it and increasing the air density, which causes the front of the moving stock's pressure to increase. Additionally, the air in the moving train set's rear area expands as a result of the vortex coming from the back, causing the air density there to decrease. As a result, the pressure on the rear portion of the moving train set is reduced.

As seen in Figure 8, there is flow separation at the area close to the top of the rear car's nose, where the plasma excitation region can be changed to reduce the local boundary layer separation. Figure 8 shows that flow separation occurs in the rear car of the rolling stock near the window position. This, combined with the velocity contour diagram of the longitudinal section, creates a significant area of low pressure behind the rear, which raises the pressure differential between the front and rear of the rolling stock and then adds to the differential pressure drag during the rolling stock travel process.

Reduce the negative pressure effect of the rear vortex. As shown in Figure 9, illustrating the rear car surface streamline, rolling stock rear nose rear area, and the nose of the two sides of the region, there is a large volume of vortex, and the rear vortex generates a low-pressure area that will increase the differential pressure drag of the rolling stock, so it should be set up in the rear car nose as well as the nose around the plasma excitation area, so that the rear area produces a jet, which can reduce the differential pressure drag.

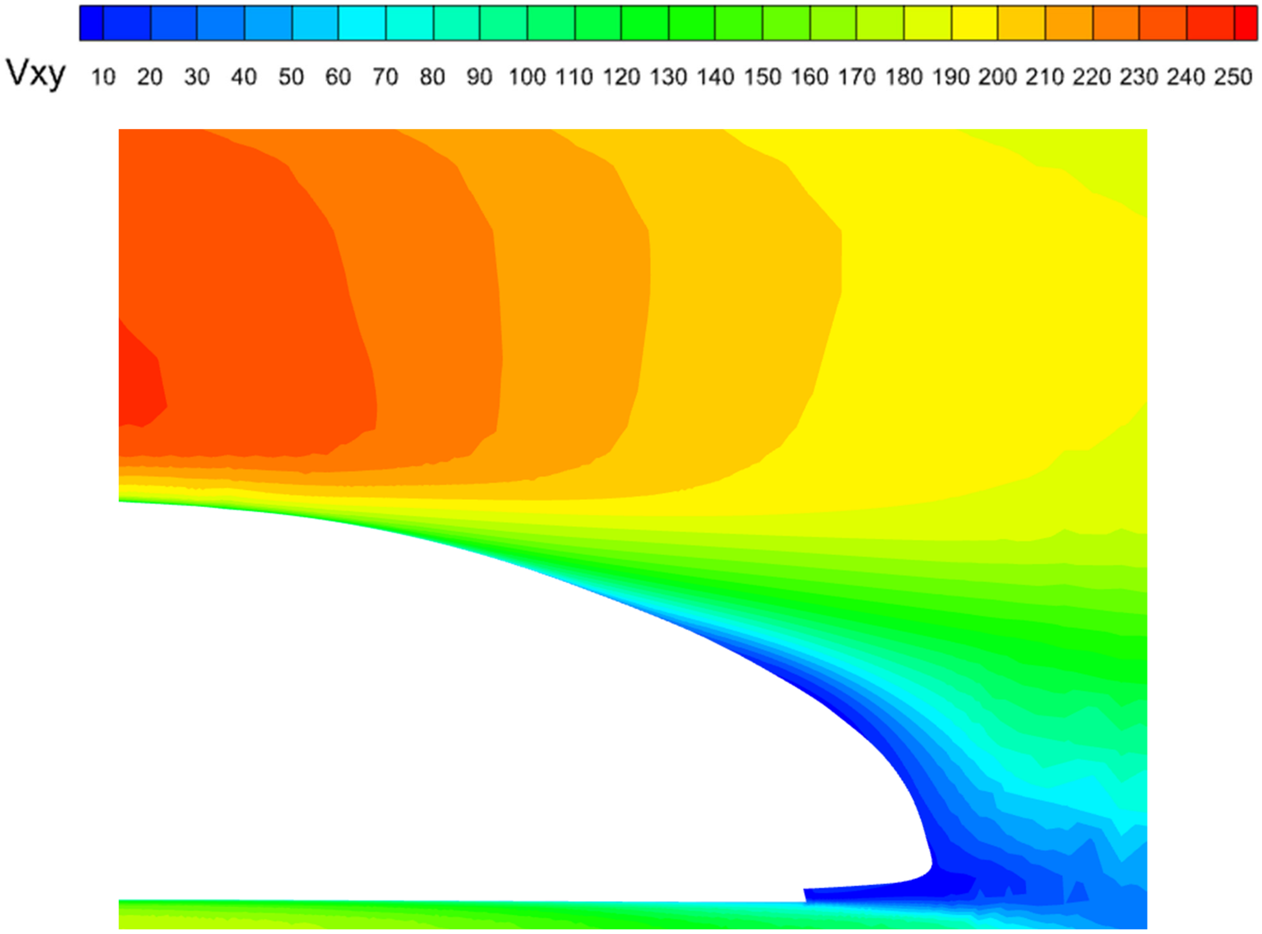

Figure 8. Velocity contour for longitudinal mid-section of the rear car.

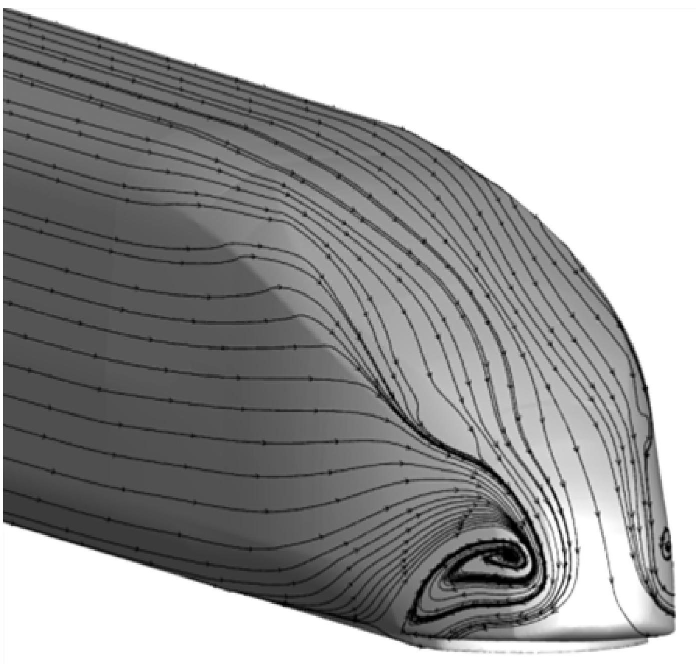

Figure 9. The rear car surface streamline.

4. Analysis of Results

The plasma excitation active control method and wake jet active control method have similarities and differences, mainly in the flow field, to impose the appropriate perturbation mode, through the local energy input to change the local flow field, so as to achieve significant improvements in aerodynamic performance, mainly including transition of delayed/accelerated flow, weakening/strengthening the turbulence vortices, promoting or inhibiting boundary layer or flow separation, and so forth. The above places can be examined for drag reduction based on the turbulent flow field surrounding the high-speed train set of the model utilized in this work. Table 5 displays the particular components of each excitation position in the rear car.

Table 5. Description of each excitation position.

Position Number	Excitation Position
Position 1	Position of flow separation above the front windshield of the rear car, between the equal-section body and streamlined rear portion of a moving train
Position 2	Upstream flow separation on both sides of the tailgate windshield
Position 3	Flow separation around the tip of the nose
Position 4	nasal tip where the rear vortex falls off

4.1. Position 1

As seen in Figure 10, position 1 is composed of a rectangular slit, which curves alongside and fits the train's surface. In Figure 11, when the moving rear end of the train, position 1, is excited at different speeds, the variation curves of the aerodynamic damping rate of the rear car and the entire train with the jet velocity are displayed.

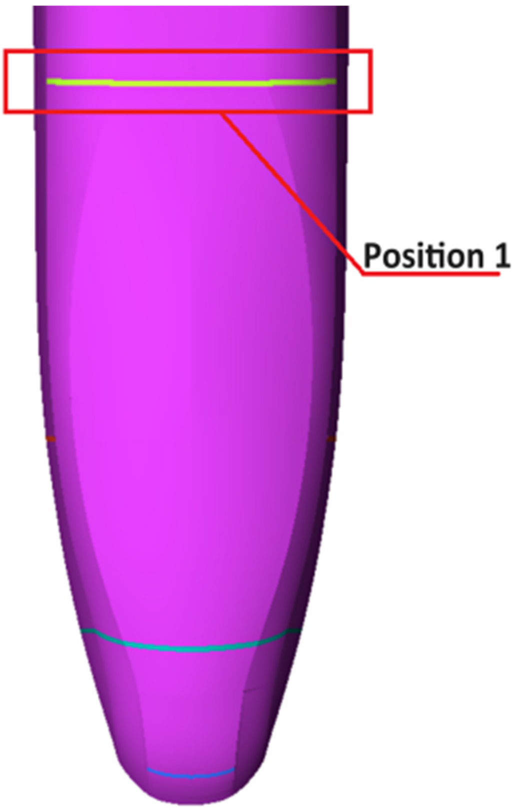

Figure 10. Position 1 schematic diagram.

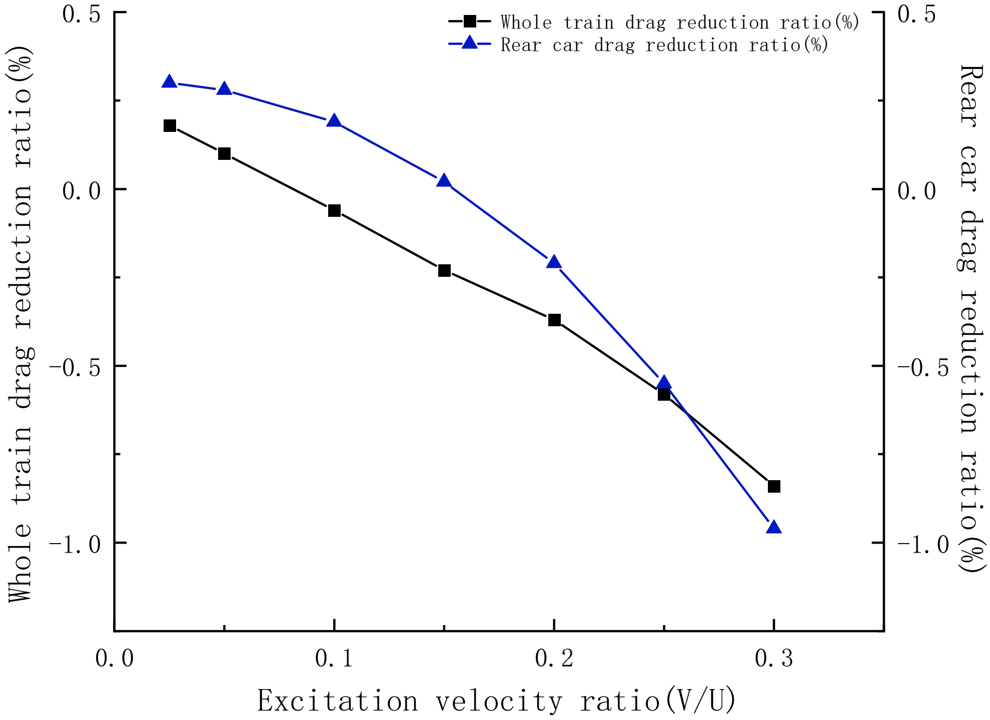

Figure 11. Drag reduction ratio variation curve with position 1 excitation speed for moving train.

When in position 1, only V/U (V for the excitation speed) < 0.05 speed jet shows a drag reduction effect, and when V/U = 0.025, the drag reduction ratio is the largest. When the rolling stock is 600 km/h, the speed operation of the rear car and the entire train drag reduction ratio are 0.3% and 0.18%, respectively, which is greater than the typical excitation speed drag reduction ratio.

When the dynamic group running speed is increased, the dynamic group pneumatic drag reduction ratio under the excitation speed gradually decreases and even seems to increase the trend of drag. On the other hand, when the dynamic group excitation speed is increased, the dynamic group pneumatic drag reduction ratio under the excitation speed is gradually reduced and even appears to decrease.

Figures 12 and 13 illustrate the pressure coefficient distribution on the surface of the rear train, the center longitudinal profile velocity contour, and the streamlines when seven excitation speed jets are generated at position 1.

Figures 12 and 13 show that for position 1, when the excitation velocity ratio increases, the area of the low-pressure area behind the excitation position progressively grows, and the aerodynamic drag caused by the low pressure at the rear gradually grows. As a result, the rear of the car experiences a delay in flow separation, flow adhesion is inhibited, the value of the low-pressure area at the back of the car is decreased, and the drag induced by the reduced value of positive pressure at the back of the car is increased. The effect causes position 1 of the plasma excitation active control to gradually lose its ability to reduce drag as the excitation speed rises. In conclusion, it can be observed that the drag reduction impact is optimum when position 1 generates a low excitation speed (V/U = 0.025).

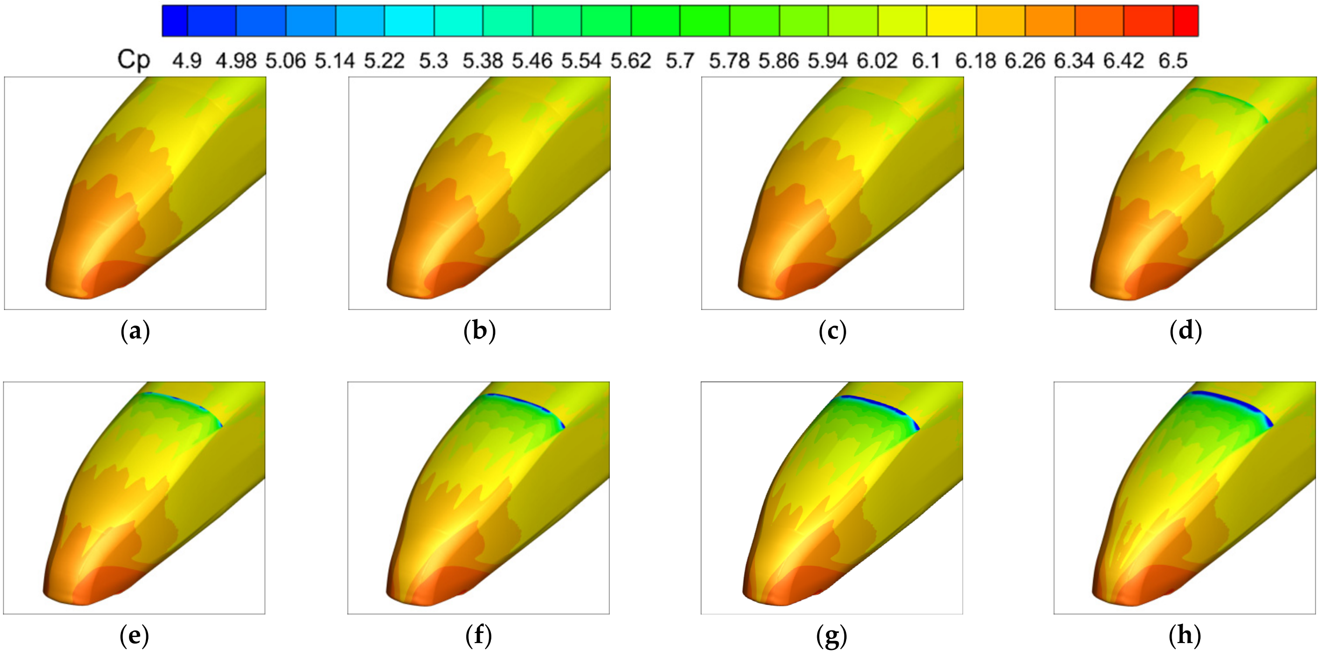

Figure 12. Variation surface pressure coefficient of the rear car with different excitation velocity ratios at position 1: (**a**) V/U = 0; (**b**) V/U = 0.025; (**c**) V/U = 0.05; (**d**) V/U = 0.1; (**e**) V/U = 0.15; (**f**) V/U = 0.2; (**g**) V/U = 0.25; (**h**) V/U = 0.3.

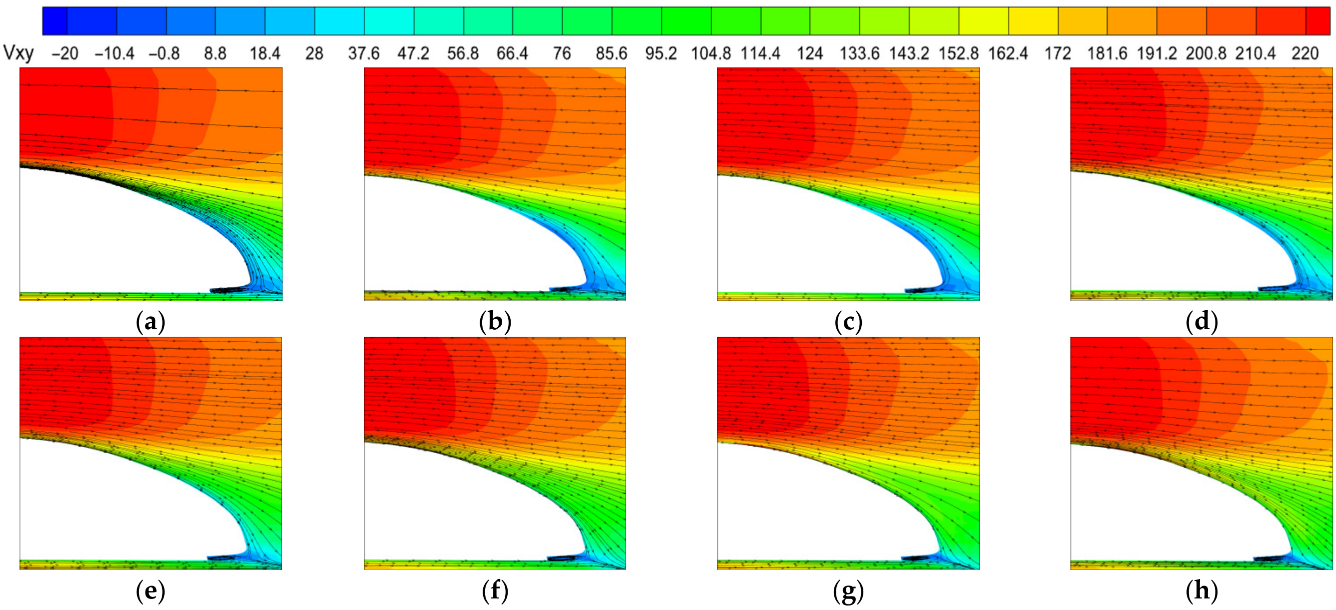

Figure 13. Position 1 center longitudinal profile rear train velocity contour and streamline diagrams: (**a**) V/U = 0; (**b**) V/U = 0.025; (**c**) V/U = 0.05; (**d**) V/U = 0.1; (**e**) V/U = 0.15; (**f**) V/U = 0.2; (**g**) V/U = 0.25; (**h**) V/U = 0.3.

Figure 14 shows the wall shear stress distribution of the moving train rear car at position 1 when the plasma device produces different excitation speeds. It can be seen that when the plasma device does not produce excitation, the lower-shear-stress region of the rear car wall is concentrated at the rear car window and nose tip positions. As the excitation speed increases, the lower-shear-stress region is also gradually expanded, the wall shear stress in this region decreases, the excitation velocity ratio V/U = 0.05, the low-stress region at the window and the low-stress region at the nose tip are correlated, and at this time, it reaches the minimum value of the wall shear stress. The excitation speed is increased again, then the wall shear stress does not decrease, but rather increases, and the wall shear stress is lower in this region. The region of lower wall shear stress decreases rapidly.

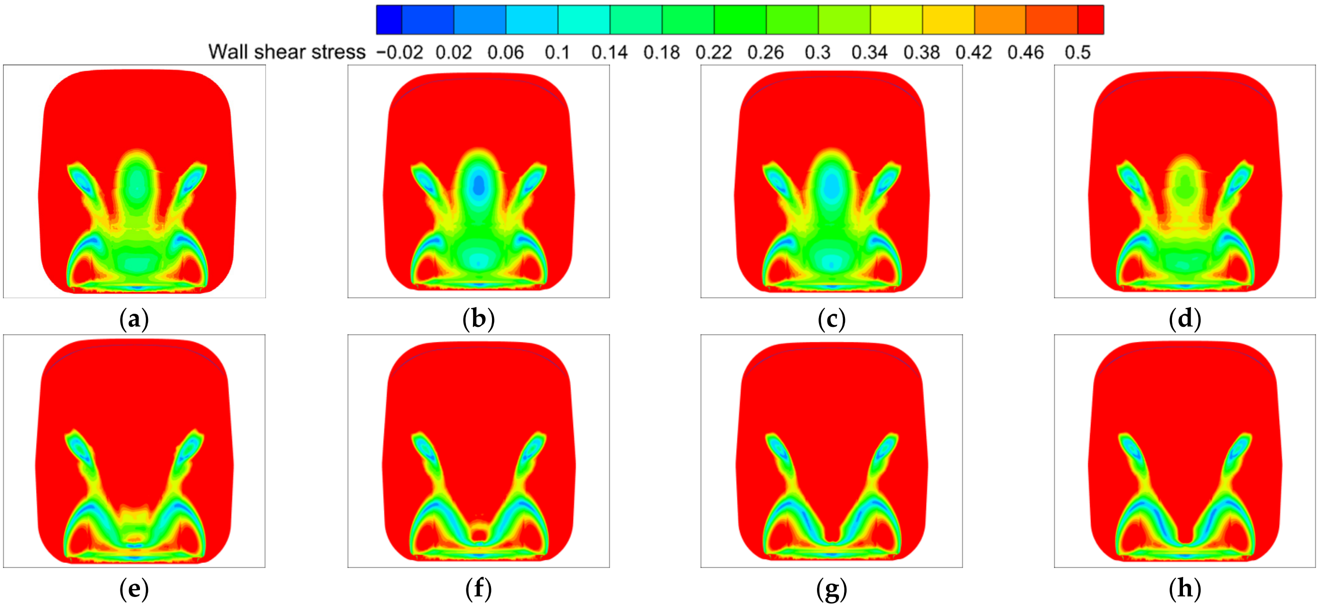

Figure 14. Distribution of shear stress on the rear car's wall surface at position 1: (**a**) V/U = 0; (**b**) V/U = 0.025; (**c**) V/U = 0.05; (**d**) V/U = 0.1; (**e**) V/U = 0.15; (**f**) V/U = 0.2; (**g**) V/U = 0.25; (**h**) V/U = 0.3.

The aforementioned phenomenon is caused by the excitation jet generated at position 1, which raises air velocity close to the boundary layer of the rear window, both sides of the window, and the tip of the nose, thereby increasing the shear force of the air on the flow field inside the boundary layer, resulting in a significant increase in wall shear stress at the window, both sides, and the nose tip.

4.2. Position 2

As shown in Figure 15, position 2, fitted to the train's surface, consists of two symmetrical trapezoidal slits with sloping edges facing upward. The variation curves of the aerodynamic drag reduction ratio of the rear car and the entire train with the jet velocity are shown in Figure 16 along with the increase in the excitation speed, when the rear car position 2 of the moving train is excited at different speeds.

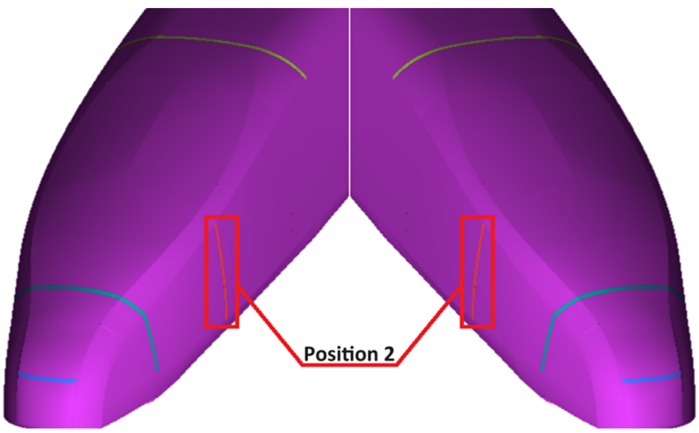

Figure 15. Position 2 schematic diagram.

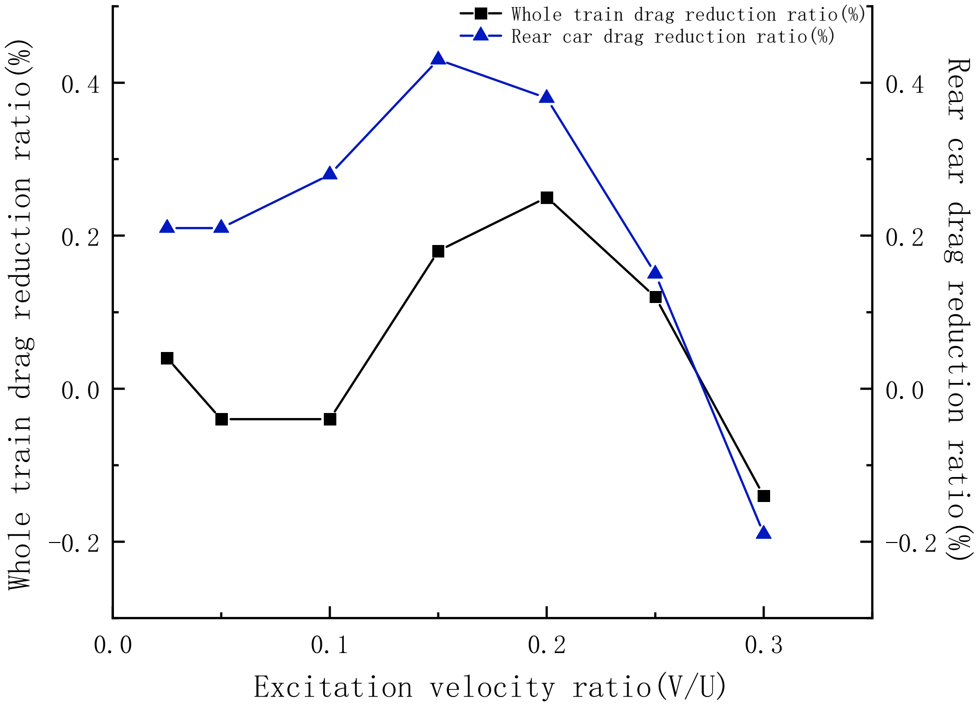

Figure 16. Drag reduction ratio variation curve with position 2 excitation speed for moving train.

As the excitation speed increases, the aerodynamic drag reduction first increases and then decreases. From the curve it can be seen that when the excitation velocity ratio is 0.1 < V/U < 0.3, there is an optimum value for both the entire train aerodynamic drag reduction ratio and the rear car aerodynamic drag reduction ratio, in which the rear car aerodynamic drag reduction ratio is the largest, with a drag reduction ratio close to 0.43%, when V/U = 0.15, and the entire train aerodynamic drag reduction ratio is the largest, with a drag reduction ratio close to 0.25%, when V/U = 0.2. V/U = 0.2 is the largest aerodynamic drag reduction ratio of the entire train, with a drag reduction ratio close to 0.25%. Subsequently, as the jet speed continues to increase, the drag reduction ratio gradually decreases. It can be seen that at rear position 2, with V/U = 0.2, the jet velocity has the best drag reduction effect.

A comparison of surface pressure coefficient distributions, center longitudinal profile velocity contours, and streamlines of the rear car at seven excitation velocity jets with the unexcited prototype in position 2 is shown in Figures 17 and 18.

As shown in Figures 17 and 18, the low-pressure region on both sides of the rear car is gradually brought closer to the rear tip along the characteristic line of the body, and the area of the low-pressure region is gradually increased as the plasma excitation velocity increases on both sides. Two symmetrical vortex zones are formed at the rear of the locomotive unit as a result of the rear air flow rate being accelerated by an increase in excitation velocity for the flow field at the rear of the rear car; additionally, the strength of the vortex zones is increased with the increase in excitation velocity, the flow reattachment is suppressed, and the value of the overpressure is further decreased.

Taking a comprehensive view at the excitation speed V/U < 0.2, the original positive pressure area positive pressure value reduction is not large, the low-pressure area does not have a wide range of coverage of the tailgate tip, and at this time, there is no obvious drag reduction effect; with the increase in excitation speed, the original tailgate flow separation of the region below the region and reattachment of the region of positive pressure value reduction of the drag increase effect is gradually obvious, so the aerodynamic drag reduction ratio with the increase in excitation jet speed shows a decreasing trend. Therefore, the aerodynamic drag reduction ratio shows a decreasing trend with the increase in the excitation jet velocity.

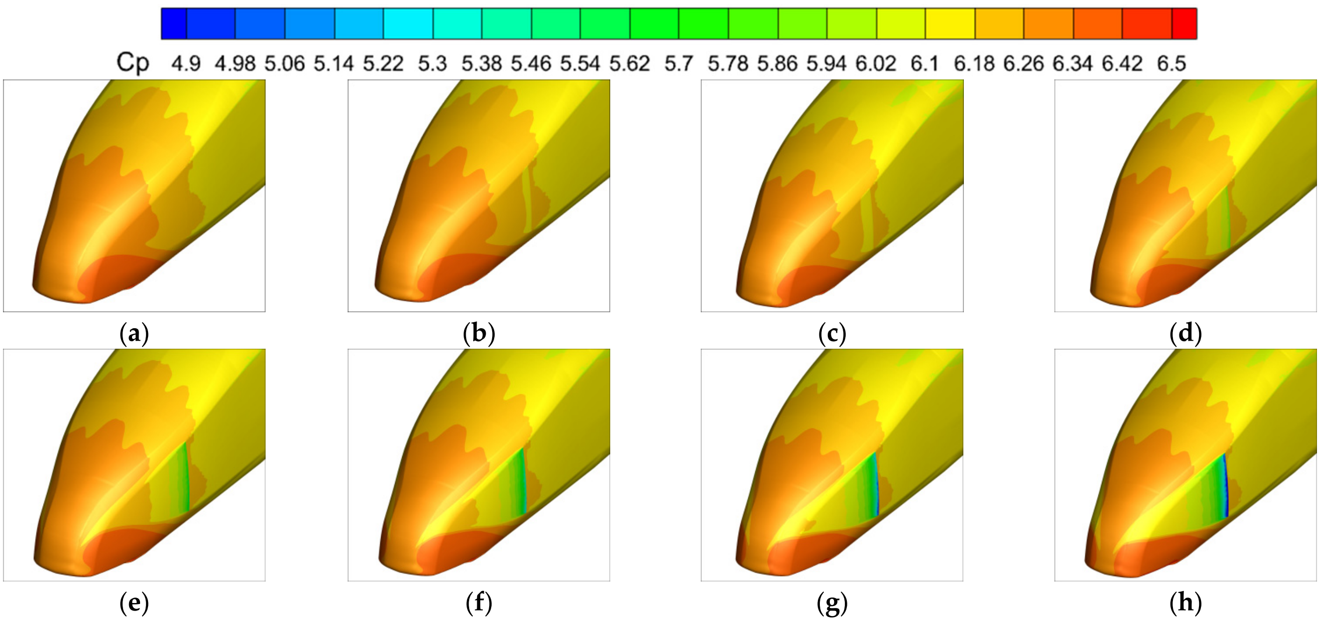

Figure 17. Variation in rear car surface pressure coefficient for different excitation velocity ratios at position 2: (**a**) V/U = 0; (**b**) V/U = 0.025; (**c**) V/U = 0.05; (**d**) V/U = 0.1; (**e**) V/U = 0.15; (**f**) V/U = 0.2; (**g**) V/U = 0.25; (**h**) V/U = 0.3.

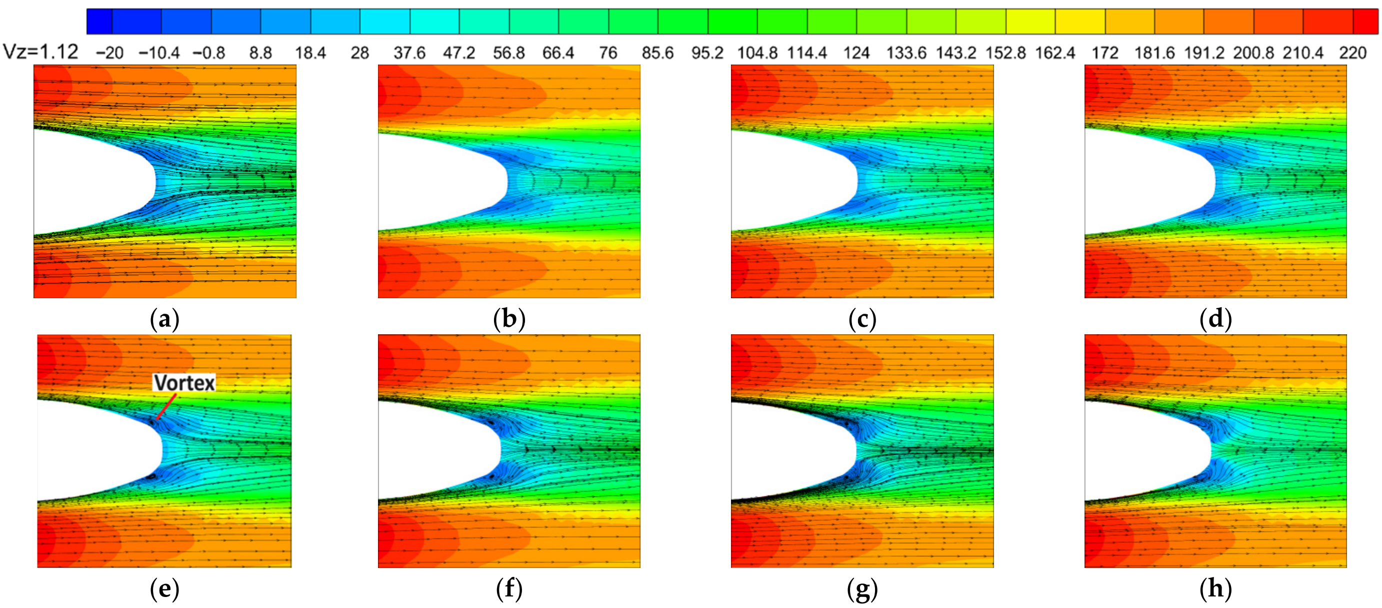

Figure 18. Velocity contour and streamline diagrams at z = 1.12 profile for position 2: (**a**) V/U = 0; (**b**) V/U = 0.025; (**c**) V/U = 0.05; (**d**) V/U = 0.1; (**e**) V/U = 0.15; (**f**) V/U = 0.2; (**g**) V/U = 0.25; (**h**) V/U = 0.3.

The distribution of wall shear stress in the rear car of a moving train at position 2 is shown in Figure 19 when the plasma device generates various excitation speeds. As can be observed, the rear car's lower wall shear stress is centered at the rear window and nose tip position when the plasma device does not provide excitation. When the excitation velocity ratio V/U = 0.2, the low-stress area at the window and the low-stress area at the tip of the nose are completely separated. At this point, the excitation speed is increased again, the wall shear stress near the window gradually increases, and the increase in the lower wall shear stress area gradually decreases.

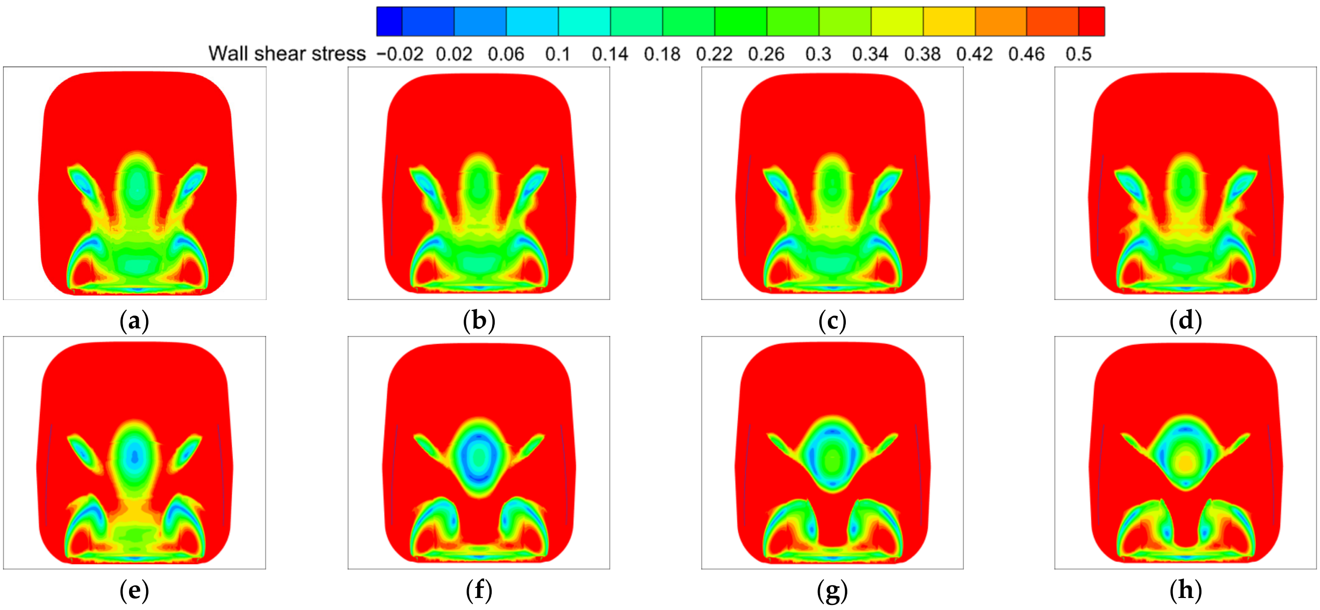

Figure 19. Distribution of shear stress on the rear car's wall surface at position 2: (**a**) V/U = 0; (**b**) V/U = 0.025; (**c**) V/U = 0.05; (**d**) V/U = 0.1; (**e**) V/U = 0.15; (**f**) V/U = 0.2; (**g**) V/U = 0.25; (**h**) V/U = 0.3.

The aforementioned phenomenon is caused by the creation of an excitation jet at position 2, which raises air velocity close to the boundary layer of the window, the window's outer sides, and the tip of the tailgate at the front, thereby increasing the shear force of the air on the flow field inside the boundary layer, resulting in a significant increase in wall shear stress at the window, both sides, and the nose tip.

4.3. Position 3

The shape of position 3 is a train's surface fitted slit, which is formed by the connection of the front and back two curves around the rear train nose, as shown in Figure 20. As the excitation speed increases for locomotive rear position 3, Figure 21 shows the variation curves for the aerodynamic drag reduction ratio of the rear car and the complete train with jet velocity.

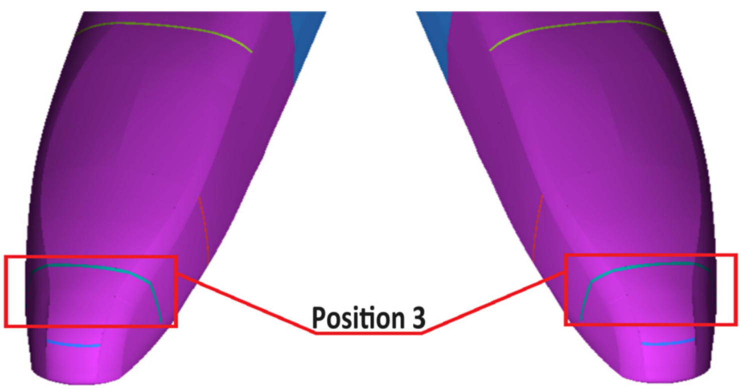

Figure 20. Position 3 schematic diagram.

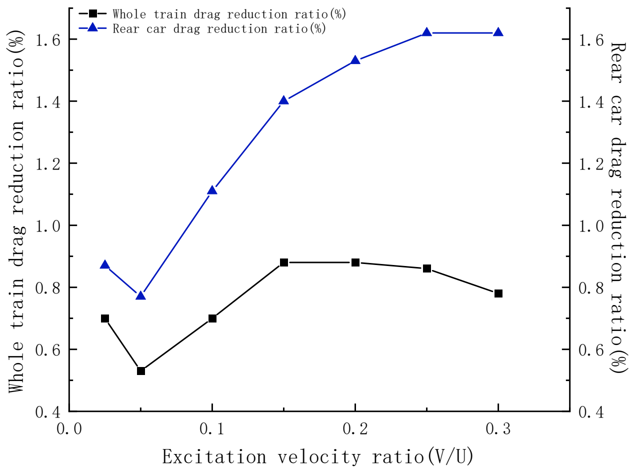

Figure 21. Drag reduction ratio variation curve with position 3 excitation speed for moving train.

With the increase in the excitation speed, the total drag reduction ratio of the rear car of the moving train becomes an upward trend, and the drag reduction ratio of the total car of the moving train reaches the maximum at V/U = 0.15 and V/U = 0.2, with a drag reduction ratio of about 0.88%; the drag reduction ratio of the rear car reaches the maximum at V/U = 0.25, with a drag reduction ratio of 1.62%, while at this time, the drag reduction ratio of the rear car reaches about 0.88%. The aerodynamic drag reduction ratio of the rear car reaches the maximum at V/U = 0.25, with an aerodynamic drag reduction ratio of 1.62%. At this time, the aerodynamic drag reduction rate of the entire train decreases with the increase in excitation speed.

At position 3, the distribution of pressure coefficients on the surface of the rear car of the moving train at different excitation velocity jets, the velocity contour and streamlines in the central longitudinal profile, and the velocity contour and streamlines at the rear car at the z = 1.12 profile (a cross-section in the z-direction is introduced to more clearly describe the changes in the flow field near the rear car) are shown in Figures 22–24 for comparison with that of the prototype car.

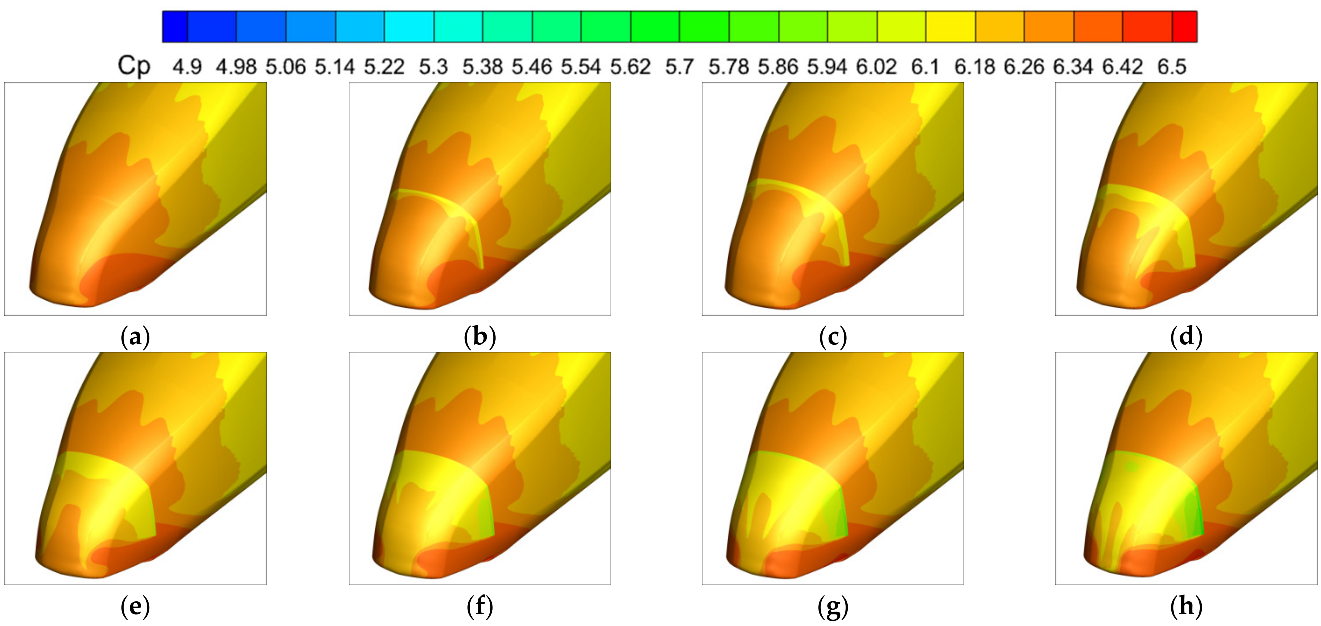

Figure 22. Variation in rear car surface pressure coefficient for different excitation velocity ratios at position 3: (**a**) V/U = 0; (**b**) V/U = 0.025; (**c**) V/U = 0.05; (**d**) V/U = 0.1; (**e**) V/U = 0.15; (**f**) V/U = 0.2; (**g**) V/U = 0.25; (**h**) V/U = 0.3.

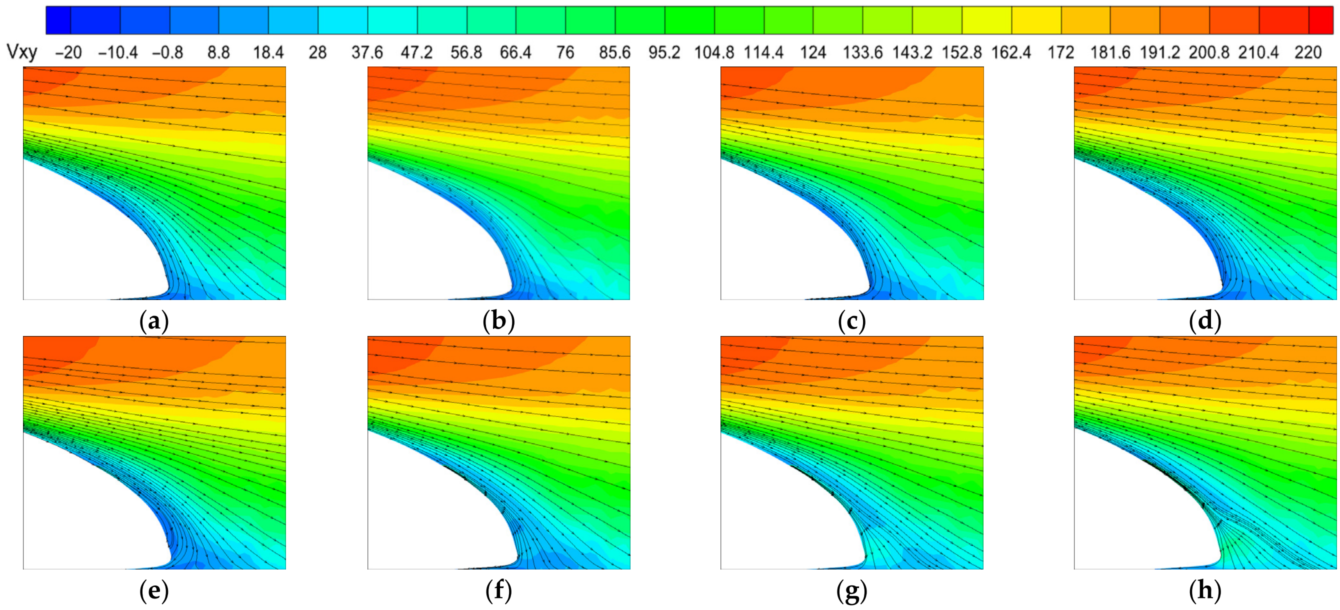

Figure 23. Position 3 center longitudinal profile rear train velocity contour and streamline diagrams: (**a**) V/U = 0; (**b**) V/U = 0.025; (**c**) V/U = 0.05; (**d**) V/U = 0.1; (**e**) V/U = 0.15; (**f**) V/U = 0.2; (**g**) V/U = 0.25; (**h**) V/U = 0.3.

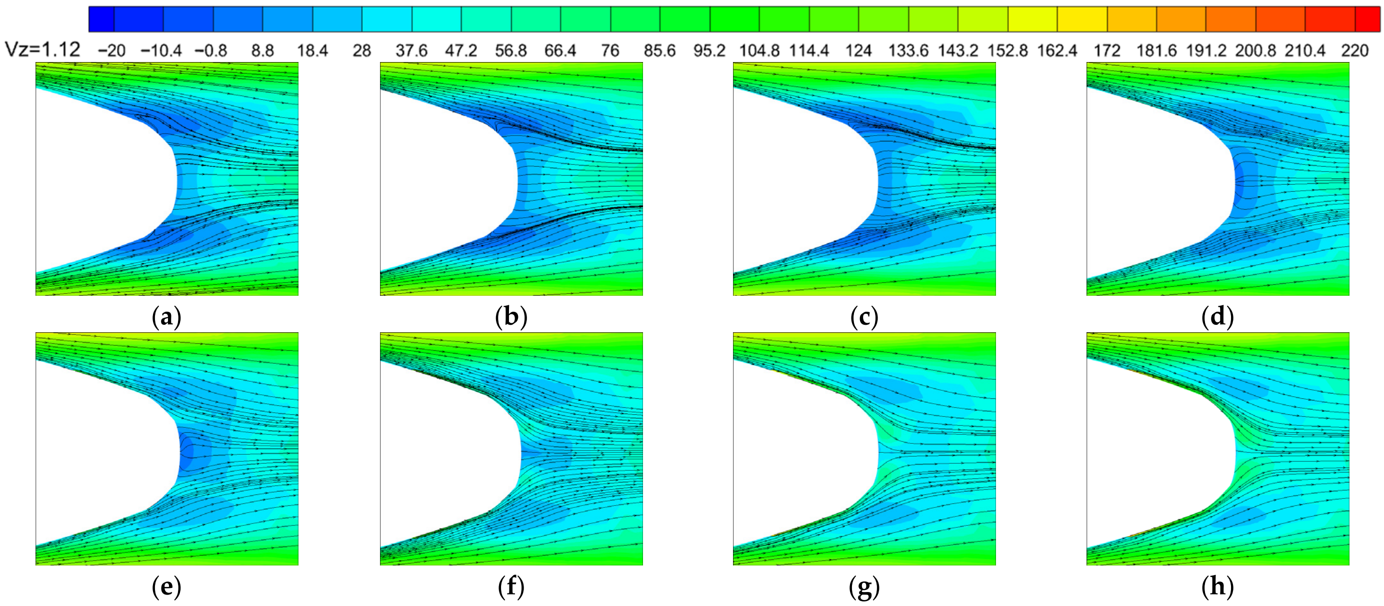

Figure 24. Position 3 velocity contour and streamline diagrams of the trailing train at z = 1.12 profile: (**a**) V/U = 0; (**b**) V/U = 0.025; (**c**) V/U = 0.05; (**d**) V/U = 0.1; (**e**) V/U = 0.15; (**f**) V/U = 0.2; (**g**) V/U = 0.25; (**h**) V/U = 0.3.

From Figure 22, when the excitation velocity ratio V/U < 0.5 at position 3, the low-pressure area generated by plasma excitation starts to appear on the rear surface pressure of the rear car, but the area is not large, so it does not have much influence on the drag reduction effect; with the increase in the excitation velocity, the area of the low-pressure area is enlarged, and the value of the positive pressure is further reduced. At the same time, with the increase in speed, the high-positive-pressure areas on the left and right sides of the nose tip of the rear car are divided by the excitation jets; at the same time, with the increase in speed, the high-positive-pressure areas on the left and right sides of the nose tip of the rear car are divided by the excitation jet, resulting in the area being reduced.

Due to the increase in excitation velocity, the acceleration of the airflow at the rear car and the velocity of the flow field behind the rear car also increase significantly. As shown in Figures 23 and 24, the acceleration of the exciter at position 3 for the air reduces the gas reflux on both sides of the nose and bottom of the rear car, which reduces the gas adhesion, suppresses the flow adhesion, and significantly improves the drag reduction ratio.

Figure 25 shows the distribution of shear stress on the rear car's wall surface at position 3 when the plasma device produces different excitation speeds. It can be seen that when the plasma device does not produce excitation, the lower-shear-stress region of the rear car wall is centered around the rear car nose tip and at the nose tip position. As the excitation speed increases, the low-shear-stress region is located near the nose tip of the rear car, and the wall shear stress in this region decreases. The low-stress region at the window and the low-stress region at the nose tip intersect, and the largest area of the low-shear-stress region is reached at this time; the excitation speed is increased again, then the wall shear stress does not decrease, but rather increases, and the area of the low-shear-stress region rapidly increases. The area of the low-shear-stress region rapidly decreases.

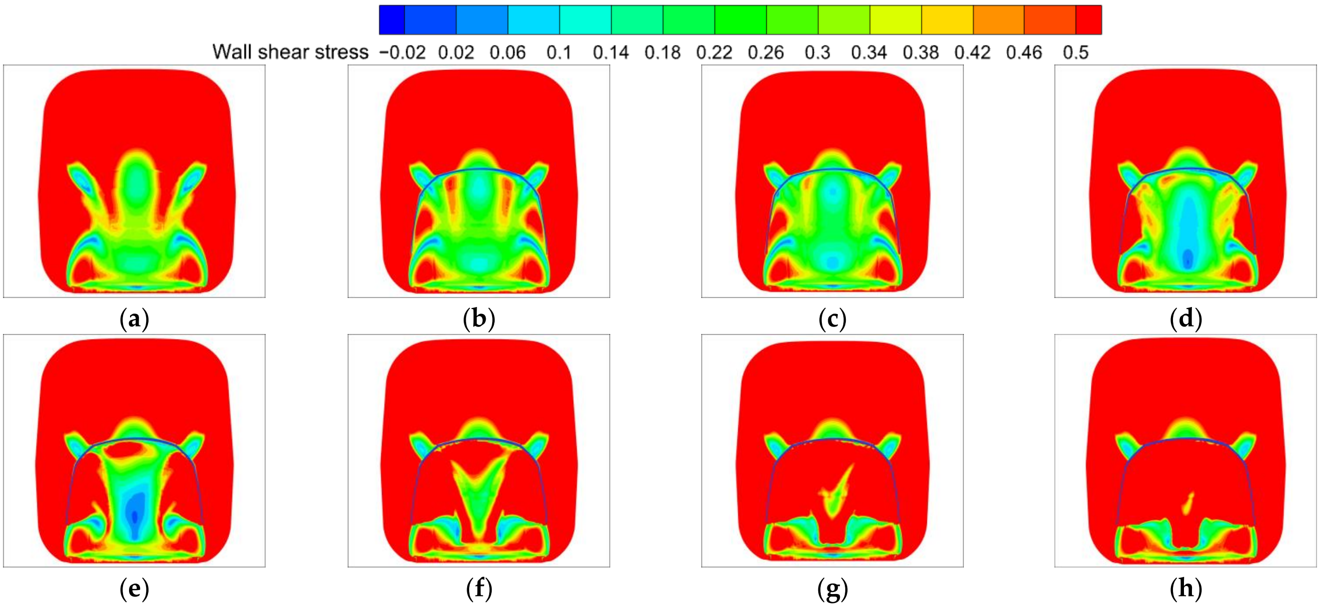

Figure 25. Distribution of shear stress on the rear car's wall surface at position 3: (**a**) V/U = 0; (**b**) V/U = 0.025; (**c**) V/U = 0.05; (**d**) V/U = 0.1; (**e**) V/U = 0.15; (**f**) V/U = 0.2; (**g**) V/U = 0.25; (**h**) V/U = 0.3.

The aforementioned phenomena are brought on by the formation of an excitation jet at position 3, which accelerates air near the boundary layer's nose tip and surrounding the rear car's nose tip. This creates a considerable increase in the wall shear stresses in this area of the rear car's nose tip and at position 3 close to the boundary layer. It also raises the air's shear force on the flow field within the boundary layer.

4.4. Position 4

As shown in Figure 26, the shape of position 4 is a rectangular train's surface fitted slit at the tip of the nose. When the moving train rear position 4 is excited at different speeds, the variation curves of the aerodynamic drag reduction ratio of the rear car and the entire train with the jet velocity are shown in Figure 27, as the excitation speed increases.

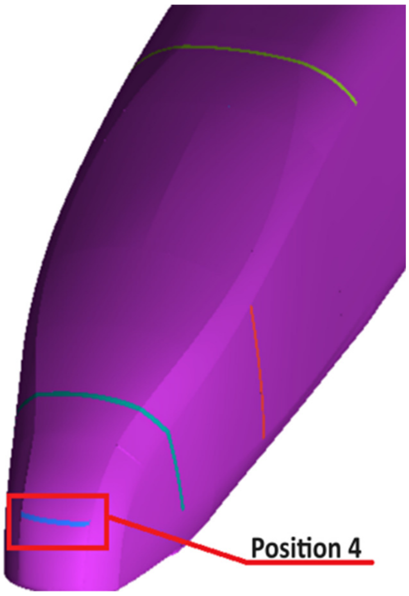

Figure 26. Position 4 schematic diagram.

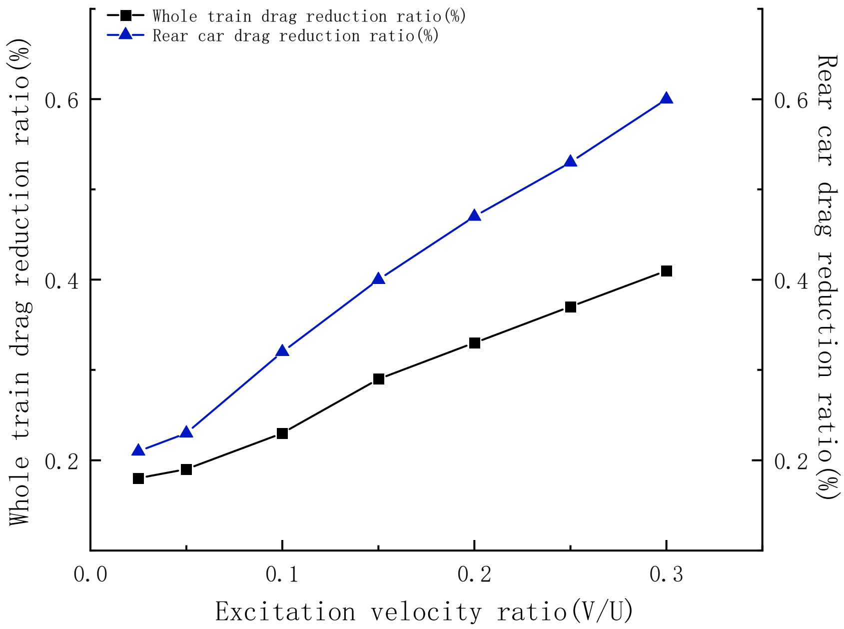

Figure 27. Drag reduction ratio variation curve with position 4 excitation speed for moving train.

With the increase in the excitation jet speed, the drag reduction ratio gradually increases, and when the excitation velocity ratio is increased to V/U = 0.3, the drag reduction ratio of the rear car and the entire train can reach 0.6% and 0.41%. When jetting at different excitation speeds, the distribution of the pressure coefficient on the surface of the rear car of the moving train, the center longitudinal profile velocity contour, and the streamline diagrams at position 4 are shown in Figures 28 and 29 for comparison with the non-excited model.

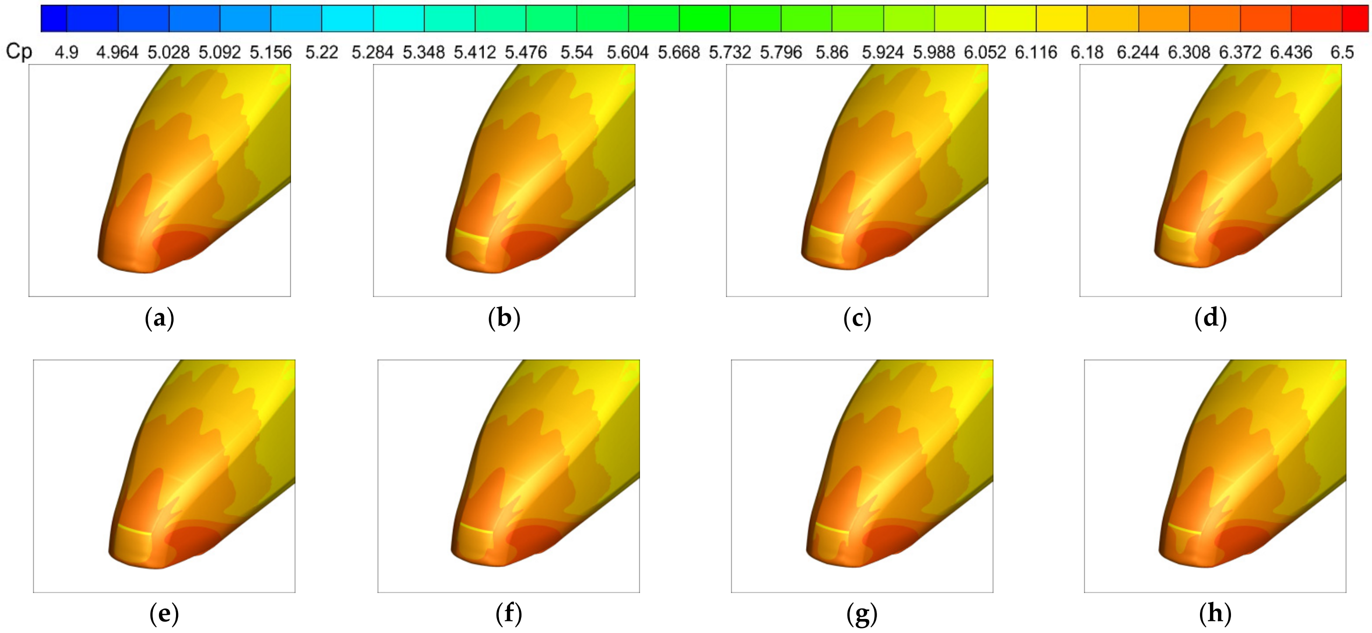

Figure 28. Variation in rear car surface pressure coefficient for different excitation velocity ratios at position 4: (**a**) V/U = 0; (**b**) V/U = 0.025; (**c**) V/U = 0.05; (**d**) V/U = 0.1; (**e**) V/U = 0.15; (**f**) V/U = 0.2; (**g**) V/U = 0.25; (**h**) V/U = 0.3.

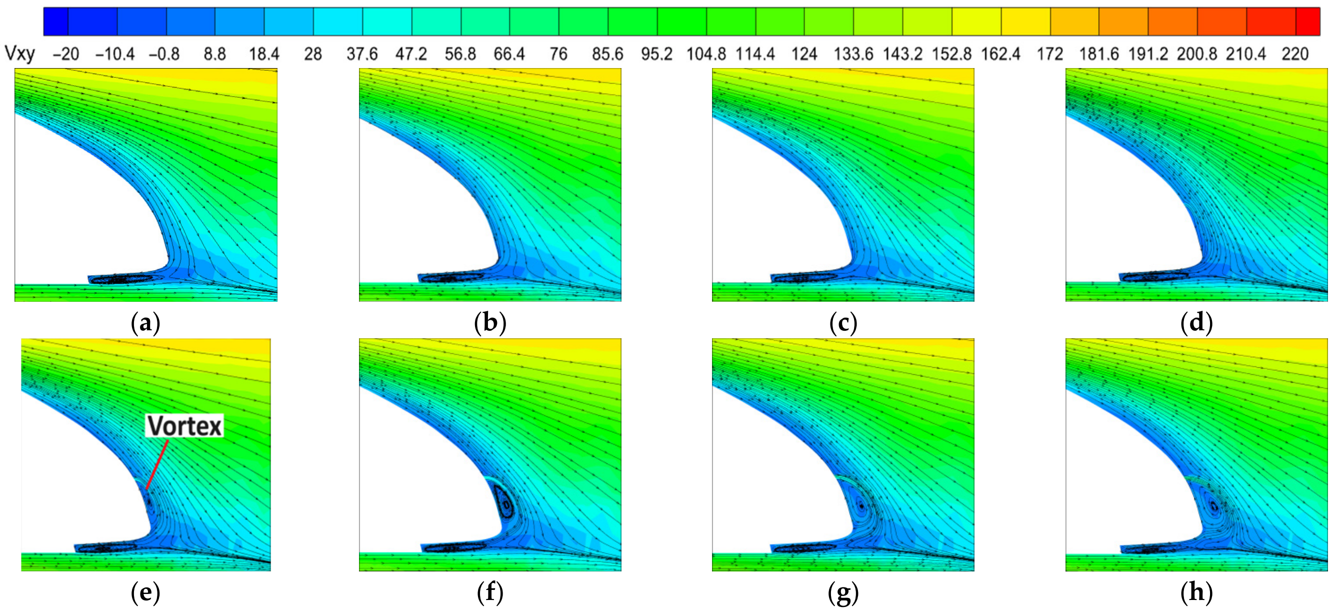

Figure 29. Position 4 center longitudinal profile rear car velocity contour and streamline diagrams: (**a**) V/U = 0; (**b**) V/U = 0.025; (**c**) V/U = 0.05; (**d**) V/U = 0.1; (**e**) V/U = 0.15; (**f**) V/U = 0.2; (**g**) V/U = 0.25; (**h**) V/U = 0.3.

As shown in Figures 28 and 29, with the increase in the excitation velocity, the surface of the car body at the tip of the rear car initially generates a small area of low-pressure positive pressure area, and with the further increase in the velocity, the low-pressure area is gradually reduced and the positive pressure value is gradually restored, and the effect of drag reduction is weakened. The flow field at the rear of the rear car has a larger vortex area, and it is continuously expanded with the increase in the excitation jet velocity. As a whole, the drag reduction potential at this position is small; the energy of the jet generated by the plasma excitation is much smaller than the vortex energy, which is insufficient to overcome the vortex energy. Overall, the drag reduction potential at this position is small; the energy of the jet generated by plasma excitation is much smaller than the vortex energy, which is insufficient to overcome the vortex to detach from the car surface, and more additional energy is consumed to improve the drag reduction ratio.

Figure 30 shows the wall shear stress distribution of the rear car of the moving train at position 4 when the plasma device produces different excitation speeds. It can be seen that when the plasma device does not produce excitation, the lower wall shear stress region of the rear car is concentrated in the rear car window and nose tip position. When the excitation velocity ratio V/U = 0.1, the low-stress area at the nose tip of the rear car develops to the maximum and then reaches the minimum value of the wall shear stress; with the further increase in the excitation speed, the low-stress area at the window and the nose tip of the rear car gradually intersect, and the low wall shear stress at the nose tip of the rear car is reduced to the minimum value. As the excitation speed is further increased, the low-stress area at the window and the low-stress area at the tip of the tailgate gradually overlap, and the area of low wall shear stress at the tip of the tailgate decreases rapidly and does not change much.

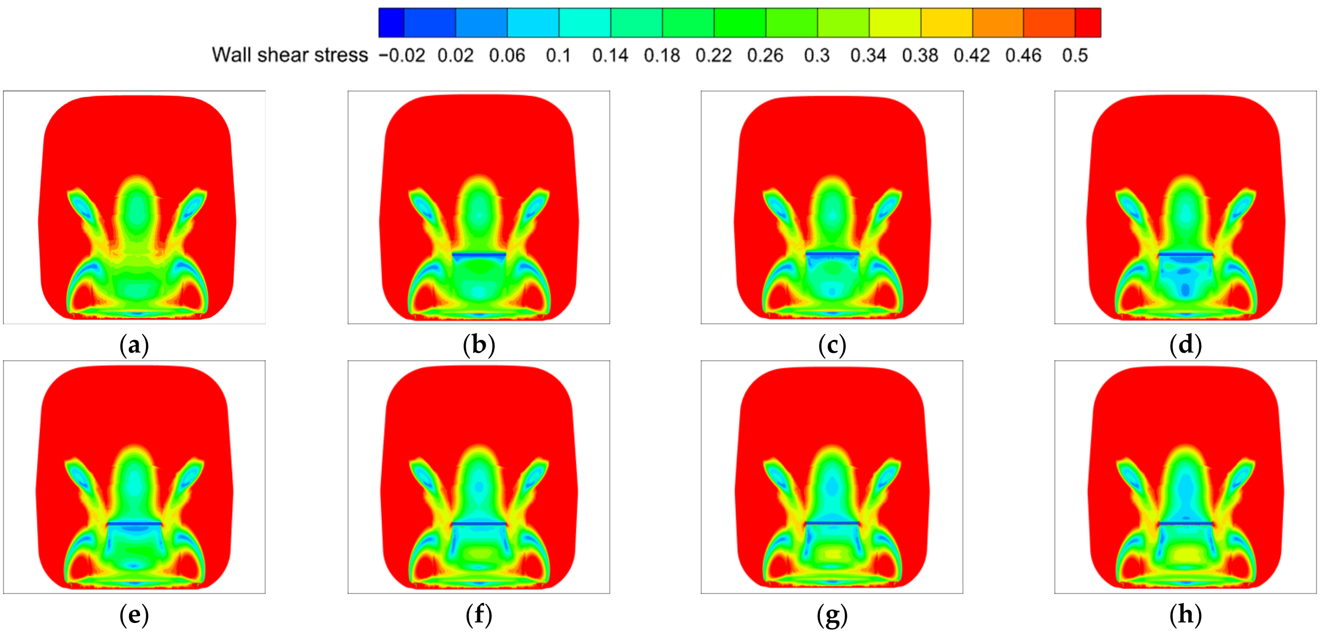

Figure 30. Distribution of shear stress on the rear car's wall surface at position 4: (**a**) V/U = 0; (**b**) V/U = 0.025; (**c**) V/U = 0.05; (**d**) V/U = 0.1; (**e**) V/U = 0.15; (**f**) V/U = 0.2; (**g**) V/U = 0.25; (**h**) V/U = 0.3.

The above phenomenon is due to the generation of an excitation jet at position 4, which results in an elevated spatial position of the vortex pair and a relative reduction in the large vortex volume range and vortex scale, thereby reducing the shear force of the air on the flow field within the boundary layer, resulting in a reduction in the wall shear stress at the nose tip position.

4.5. Comparison of Drag Reduction Effects at Four Positions

Figures 31 and 32 show the changes in aerodynamic drag of the entire train and the rear car when the absolute pressure in the vacuum tube is 10,000 Pa and the plasma excitation jets are carried out at different speeds at four positions at the rear end of the train set when the train set is travelling at a speed of 600 km/h, respectively. Overall, whether for the entire train or only for the rear car, the overall drag reduction effect is better at position 3, followed by position 4, while position 1 and position 2 have poor drag reduction effect and even drag increase phenomenon in the range of excitation speed in the paper.

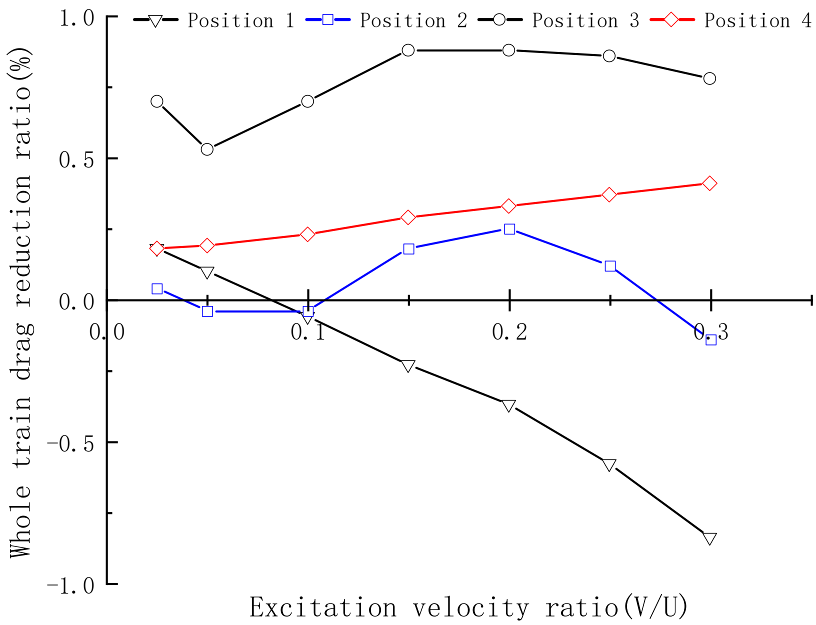

Figure 31. Whole-train drag reduction ratio for different excitation speeds at four positions.

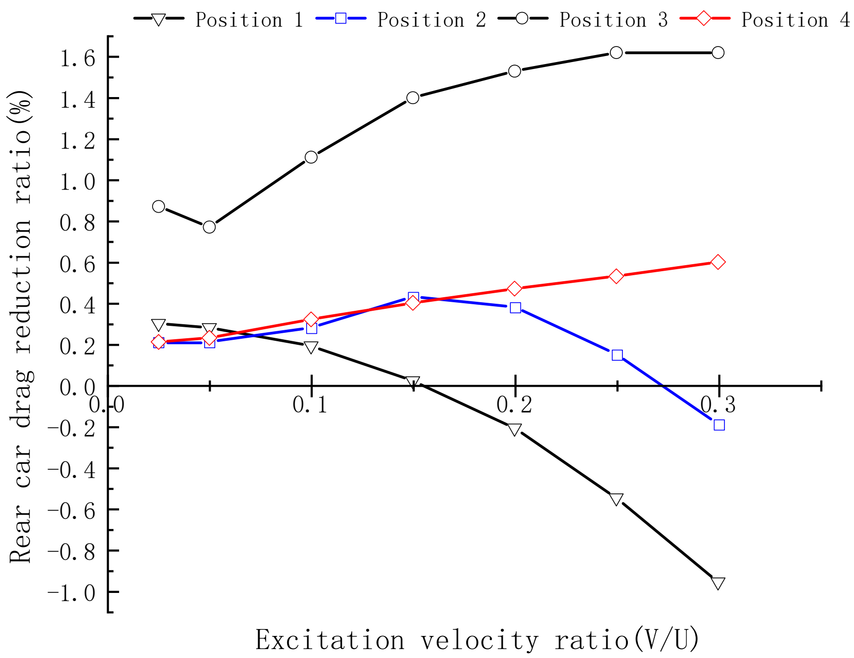

Figure 32. The rear car drag reduction ratio for different excitation speeds at four positions.

From Figure 31, it is evident that putting the plasma excitation at position 1 has no effect on reducing drag, and that as excitation speed increases, aerodynamic drag on the train increases and the drag reduction ratio for the entire train drops., which is not suitable to be the setting part of the excitation from the point of view of energy consumption, when the ratio of the excitation speed is 0. If the ratio of the excitation speed is 1 < V/U < 0.3, the best drag reduction effect occurs at the jet speed V/U = 0.2, when the drag reduction effect is at its best, and the drag reduction ratio of the entire train hits 0.25%. The maximum value of the drag reduction effect of plasma excitation is at position 2, and the best drag reduction effect occurs at this speed.

For the drag reduction situation at position 3, when the excitation velocity ratio V/U = 0.15, the drag reduction ratio of the entire train is now around 0.88%, with the excitation jet at position 3 having the best effect on reducing drag; the excitation drag reduction situation at position 4 is more considerable, and with the increase in the excitation velocity ratio, the drag reduction ratio of the entire train also increases, and it keeps an upward trend, but the improvement rate is small. In summary, it can be seen that the active control based on plasma excitation is set up at position 3 and position 4 of the rear car, which has a better drag reduction effect, and position 3 is the best from the perspective of minimizing the energy consumption of the jet.

As shown in Figure 32, for the same position, the rear car drag reduction ratio and the entire train drag reduction ratio are roughly similar, but it can be more clearly seen that position 3 belongs to the optimal drag reduction position, position 4 has a relatively large drag reduction potential, while position 1 and position 2 have a stronger drag increase phenomenon, implying an increase in train set movement speed, and are not suitable for setting up as a drag reduction position.

5. Conclusions

Based on the surface dielectric barrier discharge technology, this paper compares the effects of different electrode positions and different excitation speeds on the flow control of a vacuum tube high-speed train model.

(1) The flow control mechanism of plasma on rolling stock delays the flow separation by causing directional gas flow close to the wall, moving the flow separation point backward, reducing the size of the negative pressure zone at the end of the train's body, and reducing the pressure difference drag between the front and rear of the train's body to reduce the drag coefficient of the entire train.

(2) The best drag reduction scheme can be obtained by studying the most effective way to reduce drag. The SDBD device is installed at the flow separation around the tip of the nose, and the drag reduction effect is maximized close to the excitation velocity ratio of $V/U = 0.2$, with the drag reduction ratio of about 0.88%; the drag reduction ratio of the rear car reaches the maximum at the excitation velocity ratio of $V/U = 0.25$, with the drag reduction ratio of 1.62%.

(3) In the four positions of the excitation jet, position 4 produces the excitation jet when the rolling stock rear car wall shear stress reduction amplitude and range are larger than the other three positions to produce the excitation jet, and when the excitation velocity ratio of $V/U = 0.1$, the area of the low-stress zone at the nose tip of the rear car develops to its maximum, reaching the minimum value of wall shear stress, thereby more effectively reducing the surface friction drag of the train.

(4) Vacuum tube moving train plasma excitation drag reduction is feasible, but the maximum drag reduction ratio is not more than 2%, so the effect is weak. Due to the fact that the vacuum tube belongs to a very narrow space, its internal flow field changes are more intense and variable, so using a simple plasma excitation jet to achieve the purpose of drag reduction effect is very limited.

Author Contributions: Conceptualization, H.C. and A.L.; methodology, Y.G.; software, J.D.; validation, H.C. and Y.G.; investigation, A.L.; data curation, W.D.; writing—original draft preparation, H.C. and Y.Z. All authors have read and agreed to the published version of the manuscript.

Funding: This research was funded by the Science Researching Plans of Liaoning Provincial Education Department under Grant No. LJKZ0509 and No. LJKFZ20220203.

Institutional Review Board Statement: Not applicable.

Informed Consent Statement: Not applicable.

Data Availability Statement: Data will be made available on reasonable request.

Acknowledgments: We would like to thank the Liaoning Provincial Department of Education for providing financial support for this research. Meanwhile, we would like to thank Dalian Jiaotong University for providing the thermal engineering laboratory for this research and all the laboratory teachers for their hard work.

Conflicts of Interest: The authors declare no conflict of interest. CRRC DALIAN Co., Ltd. had no commercial interest in the publishing of this paper.

References

1. Wu, Z.; Chen, Z.; Ding, W. Optimization Design of Quasi-streamlined EMU Head Shape and Aerodynamic Performance Analysis. *J. Fudan Univ. (Nat. Sci.)* **2014**, *53*, 681–688.
2. Li, X.; Zhao, H.; Deng, W. BFOD: Blockchain-based Privacy Protection and Security Sharing Scheme of Flight Operation Data. *IEEE Internet Things J.* **2023**, 1. [CrossRef]
3. Yan, S.; Shao, H.; Min, Z.; Peng, J.; Cai, B.; Liu, B. FGDAE: A new machinery anomaly detection method towards complex operating conditions. *Reliab. Eng. Syst. Saf.* **2023**, *236*, 109319. [CrossRef]
4. Zhao, H.; Liu, J.; Chen, H.; Chen, J.; Li, Y.; Xu, J.; Deng, W. Intelligent Diagnosis Using Continuous Wavelet Transform and Gauss Convolutional Deep Belief Network. *IEEE Trans. Reliab.* **2022**, *72*, 692–702. [CrossRef]
5. Yu, M.; Pan, Z.; Jiang, R.; Zhang, J. Multi-objective Optimization Design of the High-speed Train Head Based on the Approximate Model. *J. Mech. Eng.* **2019**, *55*, 178–186.
6. Guo, D.; Wu, E.Q.; Wu, Y.; Zhang, J.; Law, R.; Lin, Y. Flight BERT: Binary Encoding Representation for Flight Trajectory Prediction. *IEEE Trans. Intell. Transp. Syst.* **2023**, *24*, 1828–1842. [CrossRef]
7. Li, M.; Zhang, W.; Hu, B.; Kang, J.; Wang, Y.; Lu, S. Automatic assessment of depression and anxiety through encoding pupil-wave from HCI in VR scenes. *ACM Trans. Multimed. Comput. Commun. Appl.* **2022**, *20*, 1–22. [CrossRef]
8. Li, M.; Zhang, J.; Song, J.; Li, Z.; Lu, S. A clinical-oriented non severe depression diagnosis method based on cognitive behavior of emotional conflict. *IEEE Trans. Comput. Soc. Syst.* **2022**, *10*, 131–141. [CrossRef]
9. Liang, Z.; Jiye, Z.; Tian, L.; Zhang, W. Multi-objective Aerodynamic Optimization Design for Head Shape of High-speed Trains. *J. Southwest Jiaotong Univ.* **2016**, *51*, 1055–1063.
10. Duan, Z.; Song, P.; Yang, C.; Deng, L.; Jiang, Y.; Deng, F.; Jiang, X.; Chen, Y.; Yang, G.; Ma, Y.; et al. The impact of hyperglycaemic crisis episodes on long-term outcomes for inpatients presenting with acute organ injury: A prospective, multi-centre follow-up study. *Front. Endocrinol.* **2022**, *13*, 1057089. [CrossRef]
11. Yan, Z.; Yang, H.; Guo, D.; Lin, Y. Improving Airport Arrival Flow Prediction Considering Heterogeneous and Dynamic Network Dependencies. *Inf. Fusion* **2023**, *100*, 101924. [CrossRef]
12. Zhou, X.; Cai, X.; Zhang, H.; Zhang, Z.; Jin, T.; Chen, H.; Deng, W. Multi-strategy competitive-cooperative co-evolutionary algorithm and its application. *Inf. Sci.* **2023**, *635*, 328–344. [CrossRef]
13. Xie, C.; Zhou, L.; Ding, S.; Liu, R.; Zheng, S. Experimental and numerical investigation on self-propulsion performance of polar merchant ship in brash ice channel. *Ocean. Eng.* **2023**, *269*, 113424. [CrossRef]
14. Yang, J.; Zhang, Y.; Jin, T.; Lei, Z.; Todo, Y.; Gao, S. Maximum Lyapunov exponent-based multiple chaotic slime mold algorithm for real-world optimization. *Sci. Rep.* **2023**, *13*, 12744. [CrossRef] [PubMed]
15. Gu, Y.; Zhou, L.; Ding, S.; Tan, X.; Gao, J.; Zhang, M. Numerical simulation of ship maneuverability in level ice considering ice crushing failure. *Ocean. Eng.* **2022**, *251*, 111110. [CrossRef]
16. Zhao, H.; Wu, Y.; Deng, W. An interpretable dynamic inference system based on fuzzy broad learning. *IEEE Trans. Instrum. Meas.* **2023**, *72*, 2527412. [CrossRef]
17. Xiao, Y.; Shao, H.; Feng, M.; Han, T.; Wan, J.; Liu, B. Towards trustworthy rotating machinery fault diagnosis via attention uncertainty in Transformer. *J. Manuf. Syst.* **2023**, *70*, 186–201. [CrossRef]
18. Chen, X.; Shao, H.; Xiao, Y.; Yan, S.; Cai, B.; Liu, B. Collaborative fault diagnosis of rotating machinery via dual adversarial guided unsupervised multi-domain adaptation network. *Mech. Syst. Signal Process.* **2023**, *198*, 110427. [CrossRef]
19. Ren, Z.; Zhen, X.; Jiang, Z.; Gao, Z.; Li, Y.; Shi, W. Underactuated control and analysis of single blade installation using a jackup installation vessel and active tugger line force control. *Mar. Struct.* **2023**, *88*, 103338. [CrossRef]
20. Song, Y.; Wang, Z.; Liu, Z.; Wang, R. A spatial coupling model to study dynamic performance of pantograph-catenary with train-track excitation. *Mech. Syst. Signal Process.* **2021**, *151*, 107336. [CrossRef]
21. Duan, F.; Song, Y.; Gao, S.; Liu, Y.; Chu, W.; Lu, X.; Liu, Z. Study on aerodynamic instability and galloping response of rail overhead contact line based on wind tunnel test. *IEEE Trans. Veh. Technol.* **2023**, *72*, 7211–7220. [CrossRef]
22. Shu, Y.; Jin, T. Stability in measure and asymptotic stability of uncertain nonlinear switched systems with a practical application. *Int. J. Control.* **2023**, *96*, 2917–2927. [CrossRef]
23. Deng, W.; Li, K.P.; Zhao, H.M. A flight arrival time prediction method based on cluster clustering-based modular with deep neural network. *IEEE Trans. Intell. Transp. Syst.* **2023**.
24. Liu, J.; Zhang, J.; Zhang, W. Analysis of aerodynamic characteristics of high-speed trains in the evacuated tube. *J. Mech. Eng.* **2013**, *49*, 137–143. [CrossRef]
25. Opgenoord, M.M.J.; Caplan, P.C. Aerodynamic design of the hyperloop concept. *AIAA J.* **2018**, *56*, 4261–4270. [CrossRef]

26. Wu, X.; Wang, Z.; Wu, T.; Bao, X. Solving the family traveling salesperson problem in the Adleman–Lipton model based on DNA Computing. *IEEE Trans. NanoBiosci.* **2022**, *21*, 75–85. [CrossRef] [PubMed]
27. Zhao, H.M.; Zhang, P.P.; Zhang, R.C.; Yao, R.; Deng, W. A novel performance trend prediction approach using ENBLS with GWO. *Meas. Sci. Technol.* **2023**, *34*, 025018. [CrossRef]
28. Jia, W.; Wang, K.; Cheng, A.; Kong, X.; Cao, X.; Li, Q. Air flow and differential pressure characteristics in the vacuum tube transportation system based on pressure recycle ducts. *Vacuum* **2018**, *150*, 58–68. [CrossRef]
29. Dong, D.; Wenjun, N.; Tao, S. A review on the state of art and future trends of atmospheric pressure low temperature plasma. *Trans. China Electrotech. Soc.* **2017**, *32*, 1–9.
30. Zhang, P.; Wang, J.; Shi, W.; Wu, Z. Experimental study on the separation control by plasma actuator in subsonic flow. *J. Exp. Fluid Mech.* **2007**, *21*, 35–39.
31. Bo, Y.; Min, S.; Mindi, B. Experimental investigation of airfoil flow separation control by dielectric barrier discharge plasma actuator. *High Volt. Eng.* **2014**, *40*, 212–218.
32. Che, X.; Nie, W.; Hou, Z.; He, H. High altitude plasma flow control simulation through ground experiment. *Acta Aeronaut. Astronaut. Sin.* **2015**, *36*, 441–448.
33. Orlov, D.; Apker, T.; He, C.; Othman, H.; Corke, T. Modeling and experiment of leading edge separation control using SDBD plasma actuators. In Proceedings of the 45th AIAA Aerospace Sciences Meeting and Exhibit, Reno, NV, USA, 8–11 January 2007; p. 877.
34. Zhou, S. Research on Aerodynamic Drag Reduction of GTS Model Based on Plasma Flow Control. Master's Thesis, Jilin University, Changchun, China, 2020.
35. Hui, Z. Research on Train Drag Reduction Based on Plasma Active Flow Control. Ph.D. Thesis, Jilin University, Changchun, China, 2020.
36. Gao, G.; Yan, X.; Peng, K. Primary research on drag reduction of train based on plasma flow. *J. Electrotechnol.* **2019**, *34*, 855–862.
37. Zhang, Y. Simulation Study on Aerodynamic Characteristics of Magnetic Levitation Transportation System with Low Vacuum Tube. Master's Thesis, Southwest Jiaotong University, Chengdu, China, 2019.
38. Zhang, K.R. Optimization of streamline structure and analysis of aerodynamic characteristics of high-speed train in restricted space. Master's Thesis, Qingdao University of Science and Technology, Qingdao, China, 2020.
39. Huang, Z.; Liang, X.; Chang, N. Numerical Analysis of Train Aerodynamic Drag of Vacuum Tube Traffic. *J. Mech. Eng.* **2019**, *55*, 165–172. [CrossRef]
40. Anderson, J.D. *Fundamentals of Aerodynamics*, 5th ed.; Aviation Industry Press: Beijing, China, 2014.
41. Shyy, W.; Jayaraman, B.; Andersson, A. Modeling of glow discharge-induced fluid dynamics. *J. Appl. Phys.* **2002**, *92*, 6434–6443. [CrossRef]
42. He, D. Analysis of Drag Reduction Mechanism and Energy Consumption of Vacuum Tube Train Suction System. Master's Thesis, Hunan University, Changsha, China, 2019.
43. Zhang, K.Y.; Li, Q.L.; Wang, C.W.; Jia, W.G. Research on aerodynamic noise of vacuum tube high-speed train. *J. Vac. Sci. Technol.* **2019**, *39*, 950–957.
44. Liu, H. Research on Comprehensive Operation Energy Consumption of Vacuum Tube Transportation System. Master's Thesis, Qingdao University of Science and Technology, Qingdao, China, 2016.
45. Liu, G.; Zhang, J.; Zhang, W. Aerodynamic drag and system parameter design of vacuum tube high-speed train. *J. Vac. Sci. Technol.* **2014**, *34*, 10–15.
46. Kim, T.K.; Kim, K.H.; Kwon, H.B. Aerodynamic Characteristics of a Tube Train. *J. Wind. Eng. Ind. Aerodyn.* **2011**, *99*, 1187–1196. [CrossRef]
47. Yang, Z.; Mao, M.; Chen, Y. Influence Laws Between Underbody Structure Parameters of High Speed Train and Aerodynamic Drag. *J. Tongji Univ. (Nat. Sci. Ed.)* **2019**, *47*, 1055–1064.